MASTERARBEIT | MASTER'S THESIS

Titel | Title

Spheroid optimization and effect of bacterial ghosts on TLR4 pathway in CT26Luc spheroids

verfasst von | submitted by

Stefanie Mayer BSc

angestrebter akademischer Grad | in partial fulfilment of the requirements for the degree of

Magistra pharmaciae (Mag. pharm.)

Wien | Vienna, 2025

Studienkennzahl lt. Studienblatt | Degree programme code as it appears on the student record sheet:	UA 066 605
Studienrichtung lt. Studienblatt | Degree programme as it appears on the student record sheet:	Masterstudium Pharmazie
Betreut von | Supervisor:	Univ.-Prof. Dipl.-Ing. Dr. Manfred Ogris
Mitbetreut von | Co-Supervisor:	Haider Sami Ph.D.

Acknowledgments

I would like to take this opportunity to thank Univ.-Prof. Dipl.-Ing. Dr. Manfred Ogris for giving me the chance to complete my master's thesis at the Laboratory of Macromolecular Cancer Therapeutics (MMCT). I have always wanted to make at least a small contribution to tumour therapy research and with his agreement I have had the opportunity to do so.

Special thanks go to Mag. pharm. Marlene Eder who supervised and supported me during this master's thesis. Thank you for always having an open ear and standing by my side even in stressful phases.

I would also like to thank my co-supervisor Dr. Haider Sami for his competent support and co-supervision, as well as his positive energy, which always created a good atmosphere in the team.

Many thanks to the rest of the MMCT team for a time that I will remember fondly for many interesting and funny conversations, as well as intensive discussions, for example about the flavour of gummy bears.

At this point, my heartfelt thanks go to my parents who always support me even if they don't know exactly what I'm doing here. Honestly, my sister Jasmin should get a special medal for her unconditional support and positive mindset – thank you for being always by my side.

I would also thank my partner Lukas Trawnicek, who has accompanied me through this stressful time over the last few months, made me laugh at the right moments and gave me inner peace.

Thank you! (*mic drop*)

Table of Content

1 ABSTRACT

Colorectal carcinoma remains one of the world's deadliest cancers highlighting the urgent need of new therapeutic approaches. Therefore, the objectives of this thesis are the optimization of three-dimensional spheroid models and investigation of the effect of bacterial ghosts on toll-like receptor 4 pathway.

Human colon carcinoma cells (HT29) and human epithelial endometriosis cells (EEC 12Z) were seeded at different densities to generate compact, uniform spheroids. Morphology, viability and necrotic core formation were evaluated by phase contrast imaging, resazurin assays and Live/Dead staining. HT29 spheroids exhibit a coronal layer and a progressively enlarging necrotic core from day 7 onwards, whereas EEC 12Z spheroids form small, compact aggregates with an early necrotic core by day 3 that plateaus. The supplementation of collagen enhances the viability of EEC 12Z spheroids slightly in contrast to gelatine-treated and untreated spheroids.

Murine colon carcinoma spheroids (CT26Luc) exposed to Alexa Fluor 488-labelled bacterial ghosts for up to 72 h demonstrate time-dependent accumulation at the periphery. Immunohistochemical analysis of sectioned spheroids reveals selective activation of TRAM-dependent toll-like receptor 4 -signalling cascade with increasing IL-6 production. No significant differences in IL-10 or pNFκB signals are visible, and the staining of the proliferation marker Ki-67 confirms proliferative zones at the periphery.

These findings validate spheroids for investigating complex tumour-immune interactions and highlight bacterial ghosts as promising toll-like receptor 4 -targeted immunomodulatory adjuvants.

Keywords: spheroid models, bacterial ghosts, toll-like receptor 4, colorectal carcinoma

2 ZUSAMMENFASSUNG

Das kolorektale Karzinom ist nach wie vor eine der tödlichsten Krebsarten der Welt, was den dringenden Bedarf an neuen therapeutischen Ansätzen verdeutlicht. Ziel dieser Arbeit ist die Optimierung dreidimensionale Sphäroid-Modelle und die Untersuchung des Effektes von „*Bacterial Ghosts*“ auf den Toll-like-Rezeptor 4 Signalweg.

Humane Kolonkarzinomzellen (HT29) und humane epitheliale Endometriosezellen (EEC 12Z) wurden in unterschiedlicher Zahl ausgesät, um kompakte, einheitliche Sphäroide herzustellen. Morphologie, Viabilität und Bildung nekrotischer Kerne wurden mittels Phasenkontrast Bildgebung, Resazurin-Assays und Lebend/Tot-Färbung untersucht. HT29-Sphäroide weisen ab dem 7. Tag eine koronale Schicht und einen sich progressiv vergrößernden nekrotischen Kern auf, während EEC 12Z-Sphäroide kleine, kompakte Aggregate mit einem frühen nekrotischen Kern an Tag 3 bilden, der dann ein Plateau erreicht. Die Zugabe von Kollagen erhöht die Viabilität der EEC 12Z-Sphäroide im Gegensatz zu den mit Gelatine behandelten und unbehandelten Sphäroiden.

Murine Kolonkarzinom-Sphäroide (CT26Luc), die bis zu 72 Stunden lang mit Alexa Fluor 488-markierten „*Bacterial Ghosts“* exponiert wurden, zeigten eine zeitabhängige Akkumulation an der Peripherie. Die immunhistochemische Analyse der geschnittenen Sphäroide zeigt eine selektive Aktivierung der TRAM-abhängigen Toll-like-Rezeptor 4 - Signalkaskade mit zunehmender IL-6 Produktion. Es sind keine signifikanten Unterschiede in den IL-10 oder pNFκB Signalen erkennbar und die Färbung des Proliferationsmarkers Ki-67 bestätigt proliferative Zonen an der Peripherie.

Diese Ergebnisse bestätigen die Eignung von Sphäroiden für die Untersuchung komplexer Tumor-Immun-Interaktionen und weisen „*Bacterial Ghosts“* als vielversprechende, auf Toll-like-Rezeptor 4 abzielende immunmodulatorische Adjuvantien hin.

Schlagwörter: Sphäroid-Modelle, bacterial ghosts, toll-like-Rezeptor 4, kolorektales Karzinom

3 ABBREVIATIONS

2D	Two-dimensional
3D	Three-dimensional
AB	Antibody
APC	Adenomatous polyposis coli
BB	Blocking buffer
BGs	Bacterial ghosts
CD14	cluster of differentiation 14
CIN	Chromosomal instability
CRC	Colorectal carcinoma
CT	Centrifuge tube
CT26Luc	Murine colon carcinoma cells with luciferase
CY3	Cyanine 3
CY5	Cyanine 5
DAMP	Damage-associated molecular patterns
DAPI	4',6-Diamidino-2-Phenylindole
DMEM	Dulbecco's modified eagle's medium
EcN	Escherichia coli Nissle 1917
EEC 12Z	Human epithelial endometriosis cells
FCS	Foetal calf serum
FITC	Fluorescein-isothiocyanate
FLM	Fluorescence microscope
HT29	Human colon carcinoma cells
IHC	Immunohistochemical
IL	Interleukin
IRF	Interferon regulatory factor
KRAS	Kirsten rat sarcoma viral oncogene homolog
LPP	Lipoproteins
LPS	Lipopolysaccharides
LRR	Leucine-rich repeats
MAPK	Mitogen-activated protein kinases

MD-2	Myeloid differentiation factor 2
MMCT	Laboratory of Macromolecular Cancer Therapeutics
MMR	DNA-mismatch repair gene
MSI	Microsatellite instability
MyD88	Myeloid differentiation primary response 88
PAMP	Pathogen-associated molecular pattern
PBS	Phosphate buffered saline
PFA	Paraformaldehyde
PGN	Peptidoglycans
PhC	Phase Contrast
pNFκB	Phosphorylated nuclear factor kappa B
PRR	Pattern recognition receptor
P/S	Penicillin / Streptomycin
RFU	Relative fluorescence units
RSZ	Resazurin
SOP	Standard operating procedure
STAT3	signal transducer and activator of transcription 3
TIR	Toll / IL-1 receptor domain
TIRAP	TIR-domain-containing adaptor protein
TLR	Toll-like receptor
TP53	Tumour protein p53
TRAF3	TNF-receptor-associated factor 3
TRAF6	TNF-receptor-associated factor 6
TRAM	TRIF-Related Adaptor Molecule
TRIF	TIR-domain-containing adaptor-inducing interferon β
UT	Untreated

4 INTRODUCTION

This chapter provides an overview of the current state of research regarding to colorectal carcinoma and the role of three-dimensional (3D) cell culture in tumour therapy studies, as well as the principles of bacterial ghosts (BGs) technology and toll-like receptor (TLR) signalling pathways.

4.1 Colorectal Carcinoma

Colorectal carcinoma (CRC) originates from the uncontrolled proliferation of epithelial cells within the colon or rectum (Hossain et al., 2022) and remains a major global health burden, ranking among the deadliest and most diagnosed cancers worldwide (Rawla, Sunkara & Barsouk, 2019). Epidemiological studies emphasize a rise in cases of disease among younger adults, while the overall incidence has declined in populations over 50 years of age (Maida et al., 2024). CRC is classified into three primary subtypes according to clinical-epidemiological characteristics: sporadic, hereditary and colitis associated. Sporadic CRC accounts for most of all cases and is caused by several somatic mutations that are triggered by environmental and lifestyle-related risk factors. Inherited CRC is caused by specific syndromes, such as Lynch syndrome or familial adenomatous polyposis, which are results of defects in DNA mismatch repair genes (MMR) or in the adenomatous polyposis coli (APC) gene. In contrast, colitis-associated CRC develops in connection with chronic inflammatory gastrointestinal diseases such as ulcerative colitis or Crohn's disease, which are triggered by persistent inflammation of the mucosa and an enhanced dysplasia-carcinoma sequence (Hossain et al., 2022).

The pathogenesis is influenced by a multifaceted interaction between genetic predisposition and environmental factors (Hossain et al., 2022). Lifestyle factors, including diet and obesity, smoking, alcohol consumption and sedentary behaviour influences epidemiological patterns, which is why high-income regions such as North America, Europe, Australia and parts of East Asia continue to be particularly affected by this disease (Rawla, Sunkara & Barsouk, 2019). Given the increasing burden of early-onset CRC, there is an urgent need to elucidate the underlying factors driving this trend. While hereditary

predispositions play a role in a subset of cases, a growing body of evidence suggests that environmental exposures, microbiome alterations and metabolic dysregulation may contribute to the rising incidence in younger populations (Maida et al., 2024).

Due to the ongoing concerning epidemiological trends of CRC, advancements in therapy are becoming increasingly important, despite the improvements already achieved through screening programs (Maida et al., 2024). The implementation of targeted therapy has revolutionized CRC treatment by directly addressing the molecular mechanisms underlying tumour progression. To fully understand this advancement, it is essential to first examine the pathogenesis of CRC, which arises through various genetic mutations, epigenetic modifications and complex interactions between multiple signalling pathways (Xie, Chen & Fang, 2020).

The most widespread mechanism driving CRC, accounting for approximately 85% of cases, is chromosomal instability (CIN). This form leads to structural and numerical chromosomal abnormalities, particularly affecting genes such as APC, TP53 and KRAS, resulting in hyperproliferation, cell cycle dysregulation and tumorigenesis. The accumulation of these mutations leads to the adenoma-carcinoma sequence (**Figure 1**), in which normal colonic epithelial cells develop into adenomatous polyps and subsequently become invasive carcinomas (Huang & Yang, 2022).

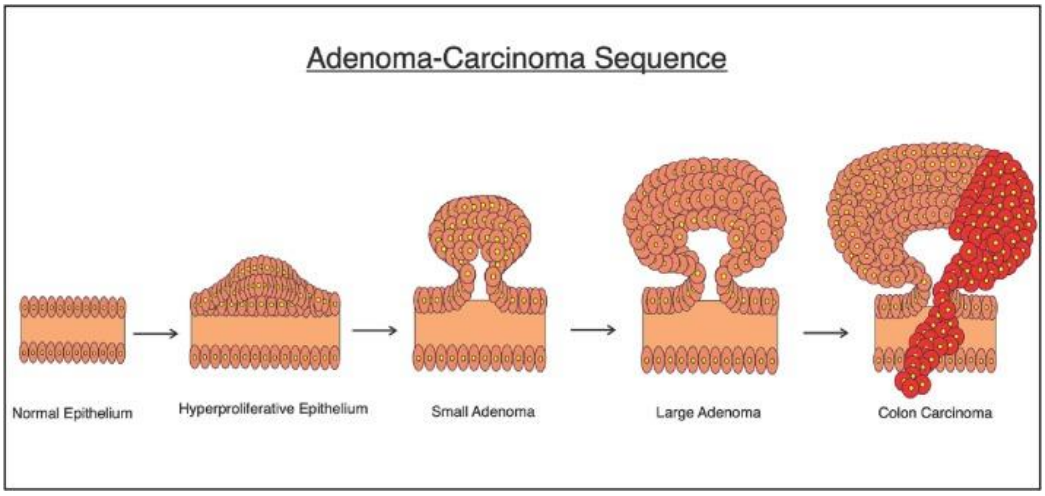

***Figure 1: Adenoma-Carcinoma Sequence**. Choudhury et al., 2023.*

A smaller subgroup of CRC cases, roughly 15 %, arises from microsatellite instability (MSI), a consequence of defects in MMR. The loss of MMR function results in the accumulation of mutations within short, repetitive DNA sequences known as microsatellites, leading to genomic instability. Unlike CIN-driven CRC, MSI-positive tumours exhibit a high mutational burden, making them particularly immunogenic and therefore responding well to immune checkpoint inhibitors.

Beyond genetic alterations, epigenetic modifications also play an important role in CRC pathogenesis. One of the most prominent mechanisms is hypermethylation of promoter regions in tumour suppressor genes, leading to their inactivation. This process is frequently associated with BRAF-V600E mutations, which contribute to CRC progression (Huang & Yang, 2022). An overview of these three molecular subtypes of CRC is provided in **Figure 2**.

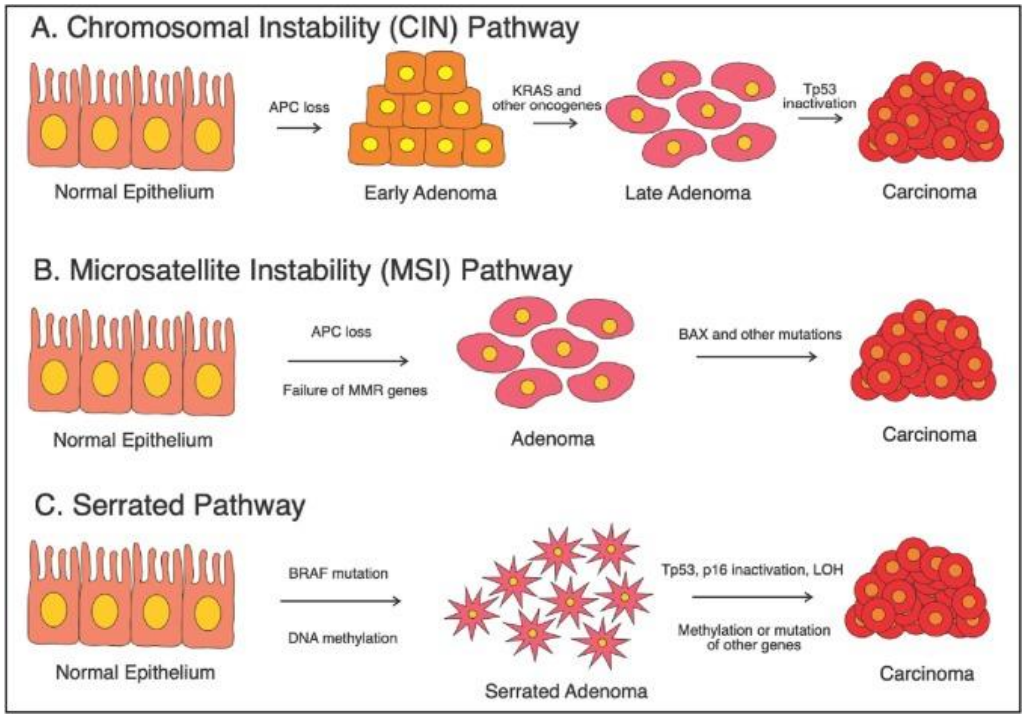

***Figure 2: Overview of molecular subtypes of CRC**, including CIN, MSI and serrated pathways. Choudhury et al., 2023.*

Understanding these distinct molecular subtypes have paved the way for targeted therapy, a treatment approach that directly interferes with specific oncogenic pathways, particularly in cases exhibiting MSI-driven tumours. Unlike conventional targeted therapies that inhibit oncogenic signalling pathways directly within tumour cells,

immunotherapy focuses on using the host immune system to recognize and eliminate malignant cells.

However, most CRC cases are driven by CINs that are resistant to checkpoint inhibitors. Therefore, research into combined therapies and the immune microenvironment of the tumour must continue (Xie, Chen & Fang, 2020).

The complex pathogenesis of CRC is extensively studied using murine colon carcinoma cell models. One widely used cell line for such investigations is CT26Luc, which has been modified to enhance its imaging capabilities. Specifically, these cells have been transduced with a retroviral vector encoding the firefly luciferase gene, enabling bioluminescent imaging for more precise tracking of tumour progression and therapeutic responses (Groza et al., 2018).

Ultimately, colorectal cancer remains a complex and evolving challenge in oncology, necessitating a multifaceted approach that integrates early detection, molecularly targeted therapy and continuous innovation in diagnostic and treatment methodologies (Xie, Chen & Fang, 2020).

4.2 Spheroids as Cancer Models

Over the last few years, 3D tumour spheroids have become a valuable tool in cancer research. Compared to two-dimensional (2D) cell culture, spheroids offer a more precise insight into the spatial characteristics of a tumour and the associated cell interactions and gene expressions. These findings can be helpful for understanding drug resistance in solid tumours (Nayak et al., 2023).

Spheroids can realistically mimic the complex tumour microenvironment and physiological conditions by developing oxygen and nutrient gradients. Depending on the available amount of nutrients and oxygen, different cell zones develop within the spheroid: necrotic, inactive and proliferative, as illustrated in **Figure 3**. The proliferative zone is located at the edge of the spheroid, as this part has the most contact with nutrients and oxygen and therefore the cell division rate is increased. In contrast, due to the diffusion restriction, the spheroid becomes increasingly hypoxic in the interior and usually develops a necrotic core (Costa et al., 2016). This zonal organization of the spheroid reflects the true conditions of the tumour microenvironment very well. Therefore, it provides insight into the efficacy of drugs at the cellular level and helps to better understand drug resistance development (Nunes et al., 2019).

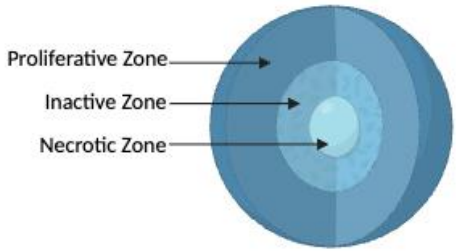

Figure 3: Cross-section of spheroid *showing different zones (proliferative, inactive and necrotic), due to nutrient and oxygen gradients. Figure adapted from Mehta et al. and created with Biorender.*

2D cell culture differs in several aspects compared to spheroid models. While spheroids consist of multilayered cell aggregates, the cells in 2D culture grow as monolayers on a flat surface. This leads to a limited cell-cell interaction and furthermore to the expression of different gene patterns than those observed in vivo. Another aspect is the formation of an extracellular matrix, which is important for understanding cell behaviour,

but which cannot be reproduced with 2D culture. Spheroids, on the other hand, can simulate the complex cellular arrangement through cell-cell and cell-matrix interactions of the tumoral environment (Costa et al., 2016). Furthermore, 2D cell culture is not zonally organised, as the cells have homogeneous access to nutrients and oxygen (Nunes et al., 2019). However, 3D cell culture also has disadvantages, such as the possible variation in structure and size per experiment, which makes it difficult to standardise experiments and compare results. In addition, the long-term culture of spheroids is limited by the lack of vascularisation and limited nutrient exchange, especially in larger aggregates (Friedrich et al., 2009).

Spheroids can be produced using either the scaffold-based or scaffold-free method. The scaffold-based approach requires external biomaterials of natural or synthetic origin to support cell adhesion and proliferation. Membranes, sponges or hydrogels provide a customisable microenvironment to facilitate cell-matrix interactions. However, it should be noted that these external structures may influence cell behaviour or drug uptake.
In contrast, no external materials are required for the scaffold-free approach, as the cells aggregate autonomously via adhesion molecules and components of the extracellular matrix if there is no other solid surface with which they can interact. There are various methods promoting spheroid formation, such as hanging drop culture, ultra-low attachment plates, rotating bioreactors or microfluidic chips. The compactness, viability and size of the spheroids are influenced by various factors, such as the cell type, seeding density and composition of the medium (Friedrich et al., 2009). In principle, the scaffold-free spheroids simulate the in vivo situation more accurate, as better cell-cell interactions are established. However, optimisation for uniform sizes is required to ensure standardisation of spheroid production (Nunes et al., 2019). As scaffold-free spheroids were produced using ultra-low attachment plates in this master's thesis, this process is shown in **Figure 4**.

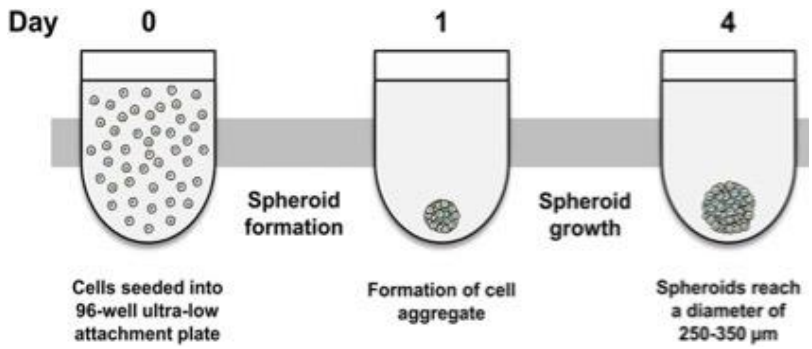

Figure 4: Scaffold-free spheroid production *using ultra-low round bottomed attachment plates. Roper et al., 2021*

The role of spheroids in modern cancer research is particularly evident in their increased use for the development of targeted and combined therapies, as well as immunomodulatory agents. Investigations such as infiltration of immune cells, cytokine diffusion and activation of immune signalling pathways are made possible by 3D cell culture. There are also other recent research goals, such as the integration of spheroids into organ-on-a-chip platforms and their use in personalised therapy tests (Nayak et al., 2023). In conclusion, spheroids serve as a bridge between simple 2D cell culture and complex animal models, with the possibility of minimising animal testing in preclinical studies. 3D cell culture enables the reproduction of essential tumour characteristic and brings helpful insights into tumour biology, having the potential to function as a testing ground for next-generation therapeutic concepts (Costa et al., 2016).

4.3 Bacterial Ghosts

Bacterial ghosts (BGs) consist of non-living, empty envelopes of gram-negative bacteria meaning that all cytoplasmic components are removed. However, the structure of the surface remains intact, and the antigenic features of the original bacteria maintains (Ijaz et al., 2024). Due to the intact surface structure, BGs can activate the cellular and humoral immune system with the help of pathogen-associated molecular patterns (PAMPs), such as lipopolysaccharides (LPS), lipoproteins (LPP) and peptidoglycan (PGN). Those PAMPs are recognized and activated by pattern recognition receptors (PRR) of dendritic cells and macrophages (Park, 2023). Particularly, LPS on the surface of BGs interact with the TLR4, while LPP and PGN activate TLR2. These interactions lead to the activation of TLR-mediated signalling pathways that induce the production of cytokines and further the secretion of pro-inflammatory interleukins. These immune mediators are important for the induction and regulation of inflammatory reactions, as well as for the recruitment of immune cells and the initiation of apoptosis (Chen et al., 2021).

These characteristics make BGs particularly interesting as drug delivery and adjuvant systems for therapeutics or vaccines (Ijaz et al., 2024). Especially for cancer research, BGs are showing enormous potential of being suitable vehicles for targeted therapy and immunotherapy, due to their ability to selectively colonize tumours (Gholami et al., 2024). In preclinical studies, BGs in combination with chemotherapeutic agents such as oxaliplatin were able to induce a significant improvement in survival and complete remissions in CRC. This effect is explained by the enhancement of immunogenic cell death mechanisms and the resulting robust T-cell activation (Groza et al., 2018). In addition, BGs are extremely promising as adjuvants in cancer vaccines, as they can induce a targeted, tumour-specific immune response by activating CD8+ T cells (Anwer et al., 2025).

BGs are produced by two main methods: genetically and chemically, as shown in **Figure 5**. The genetic method is based on the controlled expression of the lysis gene E of bacteriophages, which creates membrane pores in the bacterial cell walls and consequently releases the cytoplasm (Anwer et al., 2025). The chemical method, on the other hand, uses substances like acids, bases or detergents to induce cell lysis. The difference

between these two methods is that the genetically way is limited to gram-negative bacteria, while the chemically process functions for gram-negative and gram-positive bacteria (Salasar Moghaddam et al., 2024).

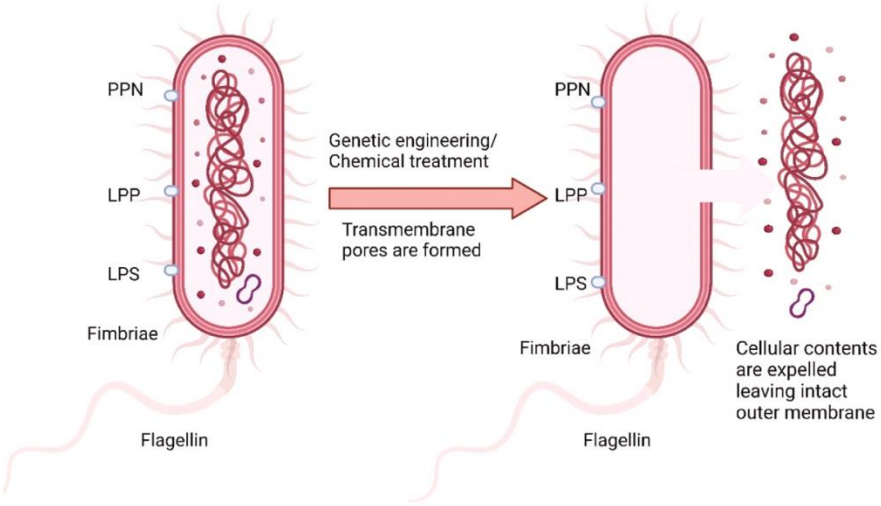

Figure 5: BG production *by pore formation via chemically or genetically methods. Afterwards, cellular contents are expelled, but the outer membrane with PAMPs stays intact. Anwer et al., 2025.*

The gram-negative bacterial strain Escherichia coli Nissle 1917 (EcN), which is already in use as a probiotic for inflammatory gastrointestinal diseases such as ulcerative colitis, is now in the focus of BG research. EcN is characterized by its low pathogenicity, genetic modifiability and its ability to selectively colonize tumours and release targeted therapeutics. However, the exact molecular mechanisms of tumour recognition and colonization are not yet fully understood. It is assumed that EcN benefits from the tumour environment, as it is poor in oxygen, rich in nutrients and immunologically more tolerant than healthy tissue. Eventually, the permeable vascular structures of necrotic areas or the adhesion through chemotaxis or specific receptors are responsible for the entrance and colonization in tumour cells (Radford et al., 2024).

However, BGs also have its disadvantages regarding to potential genotoxicity caused by colibactin, which is a bacterial toxin produced by EcN and possible residual contaminations of cellular proteins, DNA or chemicals which lead to safety concerns. Therefore, bacterial clearance and immune response need to be critically evaluated and requires detailed quality controls (Radford et al., 2024).

In conclusion, BG technology offers multiple perspectives in the field of cancer therapy, especially for personalized medicine, vaccines and targeted immunotherapy. However, further investigations are needed to ensure safety and efficacy to integrate this technology into clinical therapies (Ijaz et al., 2024).

4.4 Toll-like Receptor

The innate immune system is the body's first defence against invading pathogens, which are recognised by the PAMP-PRR interaction. TLRs are among the most studied PRRs and are therefore essential components of the innate immune system, recognising PAMPs from microorganisms and damage-associated molecular patterns (DAMPs) from stressed or dying cells (Kawai & Akira, 2010).

The activation of TLRs leads to different signalling cascades, depending on the TLR and the involved substrate. This activates various transcription factors, such as NFκB or interferon regulatory factors (IRF), which in turn trigger the production of pro-inflammatory cytokines and type 1 interferons (Heine & Riekenberg, 2009). In addition, the maturation of antigen-presenting cells is initiated, forming the bridge to the adapted immune system and resulting in the induction of an inflammatory immune response and the stimulation of antibacterial defence for the entire organism (Akira & Takeda, 2004).

To date, ten TLRs have been identified in humans, each with unique ligand specificities that determine the type of the immune response. TLRs are either located on the cell surface, where they primarily recognise extracellular pathogens, or they are localised intracellularly in endosomes to detect nucleic acid-based patterns (Kawai & Akira, 2010). **Figure 6** shows the different TLRs with their respective ligands and their localisation.

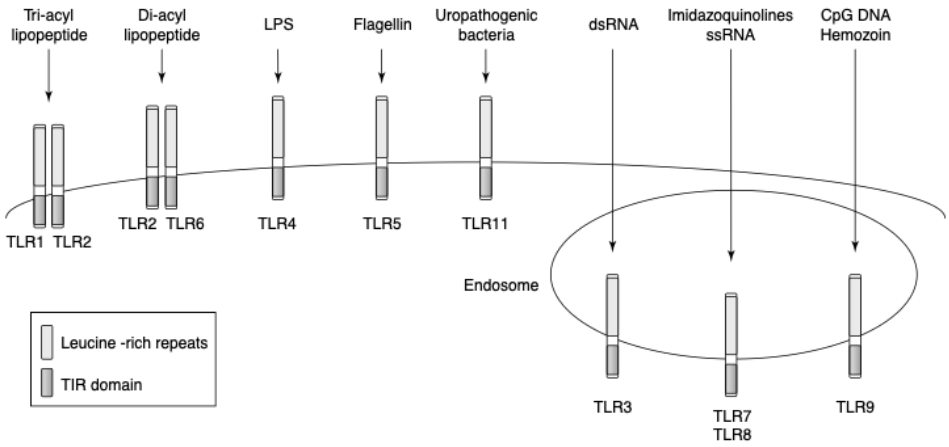

***Figure 6**: **Ligand specificities and localisation of TLRs**. TLR10 is missing, but the ligand is unclear. TLR11 is a pseudogene. Kawai & Akira, 2010.*

In the entire TLR family, TLR4 is the only one that can specifically recognise the LPS of gram-negative bacteria, which makes it particularly interesting for immunotherapy (Heine & Riekenberg, 2009). TLR4 is a transmembrane receptor that has three main domains: an extracellular domain with leucine-rich repeats (LRR), a transmembrane area and a cytoplasmic Toll/IL-1 receptor (TIR) domain. The LRR are responsible for ligand recognition, while the TIR initiates the intracellular signalling cascades (Kim et al., 2023). LPS does not bind directly to the TLR4 but forms a complex with the co-receptor MD-2 with the help of CD14 and the LPS-binding protein. This complex then binds to the TLR4 and leads to its dimerization and activation (Oblak & Jerala, 2011).

Subsequently, two different signalling pathways can be activated, which are either dependent or independent of the adapter protein MyD88 (**Figure 7**). In the MyD88-dependent signalling pathway, the Mitogen-activated protein kinases (MAPK) signalling cascade and NFκB are activated via the two adapter molecules MyD88 and TIRAP, subsequently leading to the production of pro-inflammatory cytokines (Kawaski & Kawai, 2014). In contrast, the MyD88-independent pathway is mediated via the TRIF-related adaptor molecule (TRAM) and the TIR domain-containing adaptor-inducing interferon-β (TRIF). The special characteristic of the adapter protein TRAM is its specificity to TLR4. Unlike TRIF, which is also active in the TLR3 signalling pathway, TRAM mediates the recruitment of TRIF to the receptor complex exclusively for TLR4 (Yamamoto et al., 2003). This interaction facilitates the downstream activation of various immunomodulatory genes. In principle, three paths can be initiated after uptake of the complex into endosomes using the TNF-receptor-associated factors (TRAFs):

1. Activation of IRF3 over TRAF3 and further production of interferons 1
2. Activation of NFκB over TRAF6 and further production of inflammatory agents
3. Activation of MAPKs over TRAF6 and further production of inflammatory agents (Kawasaki & Kawai, 2014).

TRAF3 is not a pro-inflammatory adapter protein, but a regulator of the immune response, thereby mediating the antiviral and immunomodulatory signalling component of TLR4 activation. In contrast, TRAF6 is strongly involved in inflammatory reactions by

activating the production of NFκB or the MAPK cascade. This results in the release of pro-inflammatory cytokines, such as interleukin (IL) 6 (Kawasaki & Kawai, 2014).

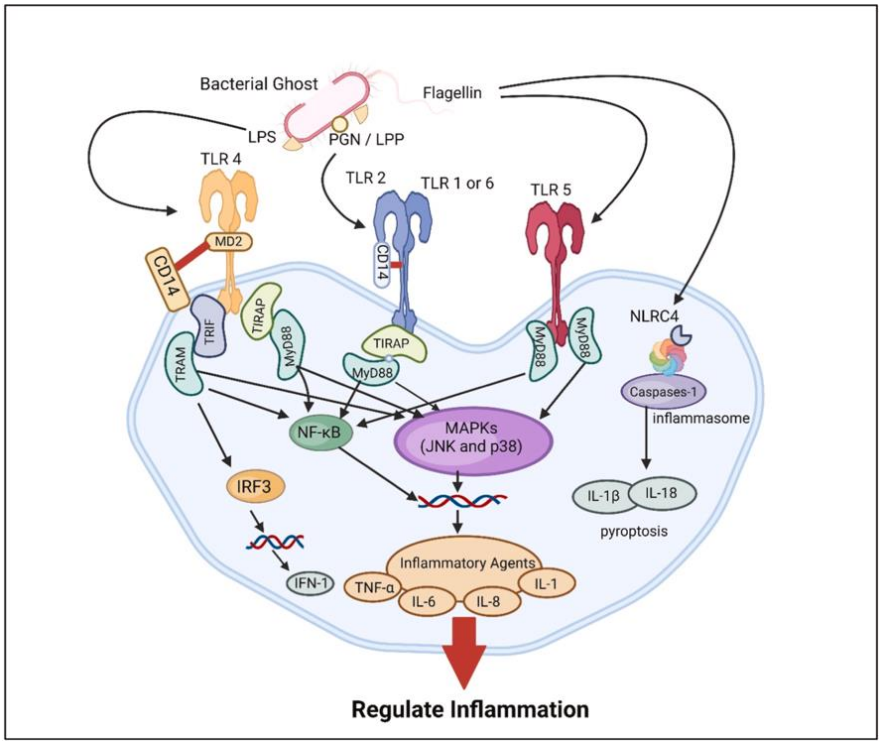

Figure 7: TLR4 pathways *with focus on MyD88-independent cascade (MAPK, NFκB or IRF3). Anwer et al., 2025.*

IL-6 is a pleiotropic cytokine involved in both innate and adaptive immune responses. Its release primarily occurs via TLR4-activation, through the classic MyD88-dependent and MyD88-independent pathways. In the MyD88-independent TRAM/TRIF pathway, the IL-6 induction happens not only via IRF3, but also through delayed activation of NFκB or STAT3, being responsible for the delayed phase of IL-6 production. This makes IL-6 a suitable functional marker for alternative TLR4-mediated immune activation (Yamamoto et al., 2003).

IL-6 is overexpressed in many tumour types, including CRC. Specifically for CRC, high IL-6 levels have been detected in both tumour tissue and serum, correlating with tumour size, metastasis and recurrence risk. Notably, IL-6 expression in CRC is associated with the activation of multiple TLRs, such as TLR1, TLR2, TLR4 and TLR8 and this cytokine induction appears to occur at least partly independent of the classic MyD88-dependent pathway (Lu et al., 2015).

IL-6 can influence almost all hallmarks of cancer (**Figure 8**) in favour of the tumour by supporting cell proliferation and angiogenesis, as well as invasion and metastasis, while suppressing apoptosis (Kumari et al., 2016). Signalling occurs mainly via the JAK/STAT3 pathway, whereby pro-survival and anti-apoptotic genes are transcribed (Chen et al., 2022). In addition, IL-6 trans-signalling via STAT3 has been shown to enhance the TLR4 response itself, which may contribute to chronic inflammatory or tumour-supportive conditions (Greenhill et al., 2011). Furthermore, IL-6 can reduce oxidative stress, activate DNA repair mechanisms and promote the expression of multidrug resistance genes, leading to the development of therapeutic resistance to chemotherapy and radiotherapy (Chen et al., 2022).

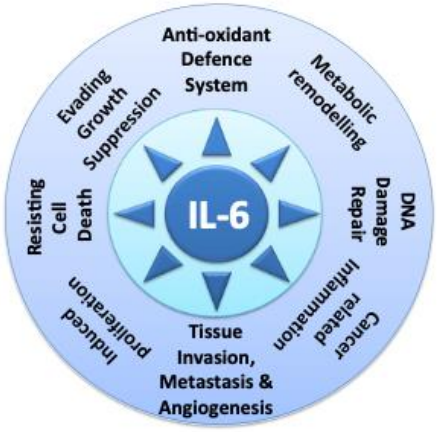

*Figure 8: **Hallmarks of cancer** and the impact of IL-6. Kumari et al, 2016*

IL-6 has not only tumour-progressive but also regenerative properties, whereby these different biological effects depend on the type of signal transduction. In classical signalling, IL-6 binds to the membrane-bound IL-6 receptor (IL-6R), which leads to anti-inflammatory effects and consequently has a regenerative effect. In contrast, IL-6 trans-signalling via soluble IL-6R and ubiquitous signalling molecule gp130 leads to pro-inflammatory and tumour-promoting effects. Therefore, trans-signalling is also possible on cells which do not express their own IL-6R, whereas the classic signalling way is restricted to cells expressing the IL-6R themselves (Greenhill et al., 2011). In summary, IL-6 is a functional marker of TRAM-mediated TLR4 activation and a key player in tumour progression, as well as inflammation regulation (Greenhill et al., 2011).

5 AIM OF MASTER THESIS

This master thesis focuses on 3D cell culture by generating spheroids of three different cell lines: human colon carcinoma cells (HT29), human epithelial endometriosis cells (EEC 12Z) and murine colon carcinoma cells (CT26Luc).

The first main goal is the optimization of spheroid formation of HT29 and EEC 12Z cells. For this purpose, the morphological structure and growth patterns are analysed using phase contrast (PhC) microscopy and resazurin (RSZ) assays to evaluate the cell viability. Due to nutrient depletion in the centre of the spheroid, they tend to establish a necrotic core with increasing size over the time. Therefore, Live/Dead staining with Hoechst and Propidium iodide is performed to investigate the necrotic core formation of HT29 and EEC 12Z. Fluorescence microscope (FLM) with a z-stack acquisition is used to get a compilation of images at different foci. Additionally, the effect of supplementation of gelatine or collagen to EEC 12Z spheroids is analysed with the aim of generating larger spheroids.

The second main objective of this master's thesis is to investigate the immunomodulatory effects of BGs on CRC spheroids, with a specific focus on the TLR4 signalling pathway in murine CT26Luc cells. The experiment aims to evaluate the uptake dynamics of BGs into CT26Luc spheroids and their subsequent impact on key components of the TLR4-mediated signalling cascade, including TRAM, pNFκB, IL-6 and IL-10. For this purpose, immunohistochemical (IHC) staining is performed utilizing a fluorescent secondary antibody (AB) for visualization. Different primary ABs relating to the specific elements of the TLR4 signalling cascade as well as the proliferation marker Ki-67.

Ultimately, this study attempts to contribute to the current understanding of BG-based immunomodulation in tumour microenvironments by using optimized 3D cell models and to assess the potential of BGs as adjuvants in cancer immunotherapy, particularly in the context of CRC.

6 MATERIALS AND METHODS

This chapter details all procedures and materials used to ensure reproducibility of the experiments, including 3D cell culture and its analysis, as well as the workflows for performing spheroid optimization and BG treatment of spheroids.

6.1 Methodological Approach for 3D Cell Culture and Analysis

In this section the methodological framework for 3D cell culture and its analysis is outlined, describing the standard operating procedures (SOP) for generating spheroids as well as performing viability and morphological assays. Subsequently, the histological processing and IHC staining of spheroids are introduced.

6.1.1 Spheroid Preparation and Culture

Generating and cultivating spheroids requires routines and multiple steps to ensure cell maintenance and uniform cell-cell aggregation. The following procedures are the groundwork of experimenting with spheroids.

6.1.1.1 Preparation of Complete Medium

The frozen additives, heat inactivated foetal calf serum (FCS), Penicillin/ Streptomycin (P/S) and L-Glutamine, were thawed in a water bath. Meanwhile, 50 mL of 500 mL medium stock were transferred into a CT-50 tube and stored in the fridge as basal medium. Afterwards, 50 mL FCS, 5 mL P/S and 5 mL vortexed L-Glutamine were added to the medium using serological pipettes. The complete medium was mixed by swirling the bottle upside down and stored in the fridge. This procedure was carried out for all the different media used for the cell culture, with the medium being dependent on the cell line.

6.1.1.2 Thawing Cells

Needed cell lines were taken from the cell bank therefore the cells had to be thawed by resuspending the cells in warm medium and transferring them into a centrifuge tube-15 (CT15). Afterwards, they were centrifuged at 200g for 5 min. The supernatant was removed, and the cell pellet was resuspended in 1 mL of prewarmed medium, transferred into a T75 flask and incubated until confluent.

6.1.1.3 Cell Splitting

Prior to initiating the splitting process, the cells cultured in T75 flasks were taken from the incubator and examined under the microscope to assess their confluency. The splitting ratio was determined based on the proportion of the flask's free surface area versus the area covered by cells. The old medium was carefully removed from the flask and the cells were washed with 5 mL of phosphate buffered saline (PBS). One to two millilitres of detaching reagent (TrypLE) were added, and the flask was incubated for a few minutes at 37° C. Once the incubation was complete, the detached cells were transferred into CT15 tubes using 7 mL prewarmed complete medium and centrifuged for 5 min at 200 g. After removing the supernatant, the cell pellet was resuspended in 1 mL of prewarmed medium. An aliquot of the resulting cell suspension, determined by the splitting ratio, was then transferred into a new T75 flask containing 12 mL medium and incubated.

6.1.1.4 Cell Counting

The remaining cell suspension was used to determine the number of cells contained in 1 mL of cell suspension. A 1:20 dilution of the cell suspension was prepared and 10 µL were transferred into each of the two counting chambers of a Neubauer Improved haemocytometer for microscopic quantification using the grid presented in **Figure 9**. The cells in the white fields were counted, while the black fields were omitted.

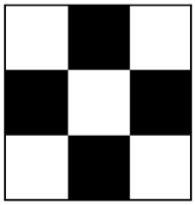

***Figure 9: Grid for cell counting**. Only cells in the white fields were counted.*

This information is necessary for calculating the required volume of cell suspension to seed specific cell densities. The counted cells were summed and averaged by dividing by 10. The average was used to determine the number of cells in the original suspension (1 mL) by using following formula:

$$c_{orig} = \emptyset * 10.000 * DF$$

c_{orig} … Cell concentration in the original suspension (cells / mL)

DF … Dilution factor

$\emptyset$ … Average of cell count in the counting chambers

Based on the concentration in the original suspension, the needed volume for the desired cell density was calculated with the following formula:

$$Volume\ of\ suspension\ needed = \frac{desired\ cell\ count\ /\ well}{cell\ count\ /\ mL\ of\ prepared\ dilution}\ X\ 1000$$

6.1.1.5 Seeding of Spheroids and Daily Procedure

For cultivating spheroids, ultra-low attachment round-bottomed 96-well-plates were used. According to individual calculations, the corresponding amount of complete medium was pipetted into the wells using a multichannel pipette. Next, the calculated amount of cell suspension was added resulting in 200 µL volume per well. As **Figure 10** illustrates, the outermost wells of the plate were filled with 200 µL PBS to ensure uniform conditions for each spheroid. Afterwards, the plate was incubated for 24 h. To ensure proper spheroid growth and adequate nutrient supply, 100 µL of old medium were removed and replaced with 100 µL new prewarmed medium from Monday to Friday. Additionally, PhC pictures of a few spheroids were captured with an Olympus IX73 microscope using a 10-x magnification.

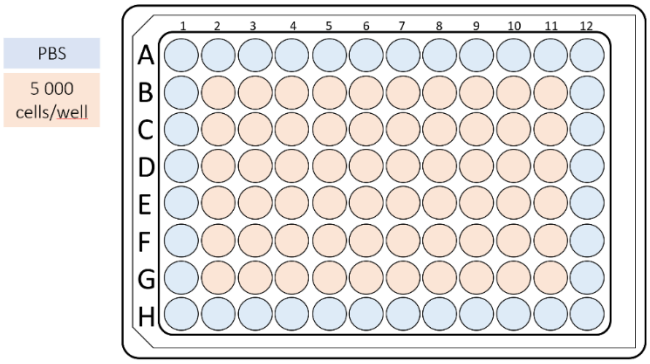

***Figure 10**: **96-well plate** with seeding scheme of spheroids. PBS = Phosphate buffered saline.*

6.1.2 Growth Analysis of Spheroids

To analyse spheroids and its characteristics such as cell viability, morphological structure and the necrotic core formation, the following three different methods were employed.

6.1.2.1 Resazurin Assay

RSZ-solution was prepared freshly for each assay. For this, 5 to 6 mg of RSZ powder were weighted with an analytical scale into an Eppendorf® tube. The powder was dissolved in PBS under light-restricted and sterile conditions with a 1 mg/mL concentration and further diluted 1:10. The dilution of RSZ was sterile filtered into a CT15 tube using a syringe filter (0.2 µm pore-diameter, polyether sulfone membrane) and a 10 mL syringe. After preparing the RSZ solution, the whole medium was removed from each well, where a RSZ assay should be performed, and replaced with 108 µL fresh prewarmed medium and 12 µL of RSZ solution. Additionally, the same was done for some of the PBS wells to gain a blank value. The plate was kept in the incubator for 4 h at 37° C. Afterwards, the plate was taken out of the incubator and 100 µL supernatant from each well were transferred to a new, flat-bottomed transparent plate. The remaining volume of the solution was removed, 200 µL prewarmed medium were added and the plate was placed back into the incubator.

Fluorescence measurements were taken using a Tecan® plate reader starting with optimal gain followed by the desired, lower manual gain. **Table 1** presents the used settings for the read-out showing different parameters and the manual gain.

Parameter	Setting
Measurement Mode	Fluorescence Bottom Reading
Excitation Wavelength	560 nm
Emission Wavelength	590 nm
Excitation Bandwith	9 nm
Emission Bandwith	20 nm
Gain	170 (Manual)
Number of Flashes	25
Integration Time	20 µs
Lag Time	0 ms
Settle Time	0 ms

***Table 1**: Parameters of Tecan® Plate Reader for analysis of resazurin assays.*

6.1.2.2 Microscopy

The spheroids were analysed with PhC and FLM using the Olympus IX73 microscope. Various images were taken with the Olympus XM10 digital microscope camera and processed with the cellSens® standard software from Olympus.

Following filters were used: PhC, DAPI, CY3, CY5 and FITC.

6.1.2.3 Live / Dead Imaging

To examine the necrotic core of spheroids, a Live/Dead staining was performed using two different staining solutions, Hoechst and Propidium Iodide (PI). Hoechst was for staining both living and dead cells and PI for dead cells. For the staining, 20 µL medium of the spheroids were removed from each well which should be imaged. 10 µL of PI and 10 µL of Hoechst were added and the plate was incubated for 2 h at 37° C. Afterwards, the spheroids were washed with PBS for three times and live-imaged using FLM with a z-stack acquisition.

6.1.3 Histological Processing of Spheroids

The cultivated spheroids were further processed to get insights into the internal and molecular architecture by sectioning and staining which is described in the following.

6.1.3.1 Harvesting and Sectioning of Spheroids

To enable further processing outside the 96-well plate, spheroids were harvested. After three PBS washes, they were carefully aspirated using a piston-operated pipette and transferred into an Eppendorf® tube. Cryomolds were pre-filled with a thin layer of Tissue-Tek® to cover the bottom before the spheroids were pipetted in and remaining PBS was removed. The disposable base molds were then placed on dry ice until solidification, followed by the addition of another Tissue-Tek® layer and storage in the freezer (-20° C). After embedding, spheroids were sectioned using a cryostat (-20° C) to obtain samples with 6 µm thickness and transferred onto Superfrost Plus™ Adhesion slides. All slides were stored at -20° C until further use.

6.1.3.2 Immunohistochemical Staining

For IHC staining, cryosectioned spheroids were encircled using a hydrophobic histology-pen to contain reagents during staining. Immediately after marking, the sections were fixed with 4% paraformaldehyde (PFA) by gently pipetting the fixative onto the marked area, followed by an incubation period of 7 minutes at room temperature. The fixative was then removed by decanting it into a designated waste container (CT-50). To remove residual Tissue-Tek®, slides were rinsed twice in PBS supplemented with 0,025 % Triton-X to enhance permeabilization, with each wash lasting 3 minutes. Following washing, the hydrophobic borders created by the histology-pen were dried using a Kimtech® wipe to prevent spreading and the slides were transferred to a prepared humid chamber lined with paper towels. To block non-specific AB binding, 25 µL of blocking buffer (BB) were pipetted onto each spheroid section. The slides were then incubated for 45 minutes at room temperature. Throughout the staining process, slides were kept in a dark chamber

whenever possible to protect fluorescent dyes from bleaching. Afterwards, the buffer was removed by tipping off the liquid.

Each spheroid was then incubated with 25 µL of primary AB targeting a specific epitope or the corresponding isotype control, diluted in BB. The slides were incubated for 120 minutes at room temperature or overnight at 4° C. Following primary AB incubation, slides were washed twice with PBS for 3 minutes per wash by pipetting approximately 1 mL PBS on each slide. The hydrophobic borders were again dried using a Kimtech® wipe. The secondary AB, diluted in BB 1:1000, was then added to each section and incubated for 120 minutes at room temperature protected from light. After the incubation, slides were washed twice with PBS for 3 minutes per wash, following the same washing procedure as before.

To counterstain the nuclei, a DAPI dilution (1 µg/mL) was added to each section and incubated for 20 minutes at room temperature. From this point forward, all steps involving DAPI required the use of nitrile gloves, as DAPI is a DNA-binding dye. After nuclear staining, slides were washed twice with PBS for 3 minutes per wash to remove excess dye and the slides were dried.

Sections were then mounted using Vectashield® antifade mounting medium, with 25 µL per slide distributed amongst the sections. Finally, the coverslips were added and sealed using nail polish to prevent drying or sample degradation before imaging. Slides were stored at 4° C until and after the imaging.

6.2 Workflow: Optimization of Spheroid Formation

Various experimental procedures based on morphological characteristics and growth patterns were used to optimize spheroid formation of human colon carcinoma cells (HT29) and human epithelial endometriosis cells (EEC 12Z). The following section outlines the workflow used for to these experiments and the detailed procedures can be found in Chapter 6.1.

6.2.1 HT29 Spheroids

The first experiment was conducted with HT29 spheroids at three different cell densities: 2500 (2.5k), 5000 (5k) and 10000 (10k). Therefore, HT29 cells with a passage number of 52 were split at a 1:10 ratio to maintain the cells in culture (using complete McCoy's 5A medium) and the remaining cells seeded in an ultra-low attachment round bottomed 96-well plate with the exact volumes and dilution factors shown in **Table 2**.

Cell amount	$V_{Suspension}$ [µL]	V_{Medium} [µL]	DF
0 (PBS)	0	200	
2.5k	33.8	166.2	1:160
5k	33.8	166.2	1:80
10k	33.8	166.2	1:40

***Table 2**: Volumes and dilution factors used for seeding HT29 spheroids at three different cell densities (2.5k, 5k, 10k). V = Volume, DF = dilution factor, k = thousand*

The experiment was later repeated to obtain more data on the growth of the spheroids but with an initial seeding number of 5k. Therefore, frozen cells (passage number of 44) were thawed using prewarmed complete McCoy's 5A medium. After one week of cultivation, the cells were split with a splitting ratio of 1:15 and seeded in a round bottomed 96-well plate. The volumes and dilution factors are presented in **Table 3**.

Cell amount	$V_{Suspension}$ [µL]	V_{Medium} [µL]	DF
0 (PBS)	0	200	
5k	32.2	167.8	1:80

Table 3: *Volumes and dilution factors used for seeding HT29 spheroids with 5k cells per well. V = Volume, DF = dilution factor, k = thousand*

The growth patterns of HT29 spheroids, represented by measuring five spheroids, were evaluated by performing six RSZ assays over a period of 23 days on alternate days for each experiment. The values were measured with the Tecan® Plate Reader using a manual gain of 170. The detailed workflow for RSZ assays is described in Chapter 6.1.2.1. Prior to executing the RSZ assay, PhC microscopy was used for taking images of the wells with a 10x-magnification.

The formation of the necrotic core was analysed using the spheroids of the first experiment to obtain information at different cell densities and time points. The procedure is explained in Chapter 6.1.2.3. The concentration of the staining solutions used and the exposure times for the microscopy can be found in **Table 4** and the preparation in Chapter 6.4.1.

Staining Dye	**Concentration (µg/mL)**	**Concentration per well (µg)**	**Exposure Time (ms)**	**Threshold**
Hoechst	320	3.2	40	500-5000
PI	500	5	10	500-16383

Table 4*: Concentration, exposure time and edited colour intensity for Hoechst and PI for visualizing the necrotic core of HT29. PI = Propidium iodide*

6.2.2 EEC 12Z Spheroids

Spheroid optimization of EEC 12Z cells was performed in several steps. In the first experiment, as with HT29, the focus was on spheroid growth using RSZ assays and analysing the formation of the necrotic core. The second experiment focused on whether the addition of gelatine or collagen affects growth, with the goal of obtaining larger spheroids.

For the first experiment, EEC 12Z cells (passage number of 43) were seeded into a round bottomed 96-well plate at three different cell densities: 5k, 10k and 20k and also kept in culture (using complete DMEM F-12 Ham medium without phenol red) with a splitting ratio of 1:15. The used volumes of the cell suspension and dilution factors are presented in **Table 5**.

Cell amount	$V_{Suspension}$ [µL]	V_{Medium} [µL]	DF
0 (PBS)	0	200	
5k	71.2	128.8	1:80
10k	71.2	128.8	1:40
20k	71.2	128.8	1:20

***Table 5**: Volumes and dilution factors used for seeding EEC 12Z spheroids at three different cell densities (5k, 10k, 20k). V = Volume, DF = dilution factor, k = thousand*

EEC 12Z spheroid growth was evaluated by performing five RSZ assays over a 16-day period, with measurements taken on alternate days from five spheroids. The Tecan® Plate Reader was utilized for measuring the values with a manual gain of 170. The Chapter 6.1.2.1 outlines the workflow for RSZ. Before each RSZ assay, PhC images of the spheroids at 10x-magnification were captured.

Table 6 lists the concentrations, exposure times and edits of the fluorescent dyes used for visualization of the necrotic core of EEC 12Z spheroids. The preparation of the staining solutions is described in Section 6.4.1 with the workflow of Live/Dead staining described in Chapter 6.1.2.3.

Staining Dye	**Concentration (µg/mL)**	**Concentration per well (µg)**	**Exposure Time (ms)**	**Threshold**
Hoechst	320	3.2	40	500-10000
PI	500	5	10	500-16383

***Table 6**: Concentration, exposure time and edited colour intensity for Hoechst and PI for visualizing the necrotic core of EEC 12Z. PI = Propidium iodide*

The second experiment investigated the impact of adding gelatine or collagen to the spheroids regarding to their growth. Therefore, EEC 12Z cells with a passage number of 29 were thawed and seeded at a density of 20k cells per well. As for the other experiment, an ultra-low attachment round bottomed 96-well plate was used to generate spheroids using a splitting ratio of 1:10. Due to limited number of cells, the undiluted cell suspension was used for cell seeding with the corresponding volumes shown in **Table 7**. For the treatment groups, cells were initially seeded in 100 µL complete DMEM F-12 Ham medium without phenol red. Final volume of 200 µL per well was reached after the treatments with collagen or gelatine.

Cell amount	$V_{Suspension}$ [µL]	V_{Medium} [µL]	DF
0 (PBS)	0	200	
20k (untreated)	13.24	186.76	-
20k (treated)	13.24	86.76	-

***Table 7**: Volumes used for seeding EEC 12Z spheroids with an initial seeding number of 20k cells per well. Untreated wells resulted in a total amount of 200 µL per well whereas treated wells resulted in a total of 100 µL due to subsequent addition of gelatine or collagen. The undiluted cell suspension was used.*
V = Volume, DF = dilution factor, k = thousand

For the comparison of gelatine and collagen supplementation to untreated spheroids, the 96-well plate was divided into different sections, presented in **Figure 11**. Spheroids on the left side of the plate remained untreated, while spheroids on the right side got treated with either gelatine or collagen.

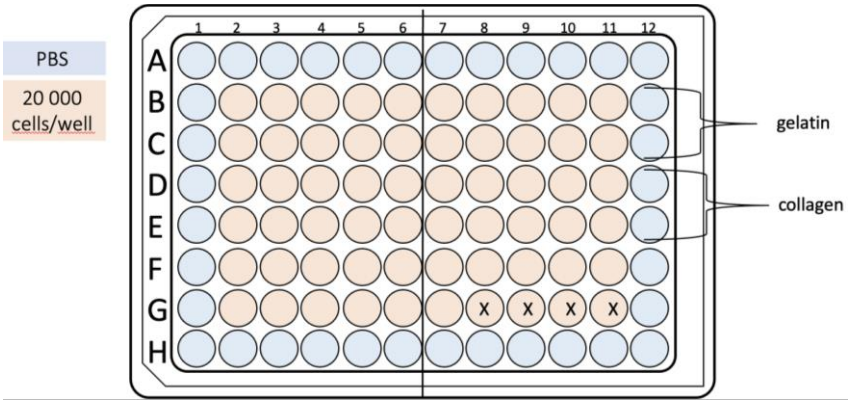

***Figure 11**: **Scheme of 96-well plate for seeding EEC 12Z spheroids** (initial seeding number of 20k cells per well), divided into untreated, gelatine-treated and collagen-treated spheroids for comparison. X = no spheroid present*

The treatment with gelatine was carried out on day 1 with an initial concentration of 0.02 %. The 2 % concentrated homemade bovine gelatine solution (described in Chapter 6.4.1) was diluted 1:50, resulting in a concentration of 0.04 %. For treatment, 100 µL of the 0.04 % concentrated gelatine solution were added to the spheroids seeded in 100 µL, resulting in a further 1:2 dilution and a total volume of 200 µL per well. Afterwards, the spheroids were incubated for 48 h. From day 3 onwards, the concentration of gelatine in the wells was thinned out by replacing 100 µL of the existing dilution in the well with 100 µL fresh medium resulting in a daily 1:2 dilution over a period of 16 days. For collagen-treatment, a 6 µg/mL concentrated collagen solution was prepared with the volumes described in Chapter 6.4.1 and added to the spheroids seeded in 100 µL in each well on day 2 post-seeding, resulting in a total volume of 200 µL per well. After the spheroids were incubated for 48 h with collagen, the concentration was thinned out using the same method as for gelatine treatment.

To investigate the impacts of collagen and gelatine supplementation on the spheroid growth, RSZ assays were performed on alternate days with the untreated spheroids as a reference. The RSZ assays were performed according to Chapter 6.1.2.1 using the Tecan® Plate Reader with a manual gain of 170. Additionally, PhC images of the different treated spheroids were taken using a 10x-magnification, prior to conducting the RSZ assays.

6.3 Workflow: BG-Treatment of CT26Luc Spheroids

CT26Luc spheroids were used to investigate the effect of BG-treatment on the TLR4 pathway by performing IHC staining. The following section provides an overview of the experimental workflow, with detailed procedures described in Chapter 6.1.

For this experiment, CT26Luc cells with a passage number of 48 were used to generate spheroids with an initial seeding density of 5k cells per well. Therefore, the cells were detached, transferred to a new flask (1:20 ratio) to keep them in culture and the remaining cell-suspension seeded into an ultra-low attachment round bottomed 96-well plate using complete DMEM F-12 Ham medium with phenol red. The corresponding volumes and dilution factors can be found in **Table 8**.

Cell amount	$V_{Suspension}$ [µL]	V_{Medium} [µL]	DF
0 (PBS)	0	200	
5k	28.8	171.2	1:80

***Table 8**: Volumes and dilution factors used for seeding CT26Luc spheroids at an initial cell density of 5k. V = Volume, DF = dilution factor, k = thousand*

Cell viability was analysed by performing seven RSZ assays on five spheroids over a 16-day period, with measurements taken on alternate days, following the protocol outlined in Chapter 6.1.2.1.

BGs derived from gram-negative bacteria (EcN) labelled with Alexa Fluor (AF) 488 were used for spheroid treatment. The seeded 96-well plate was divided into treated and untreated groups, with two spheroids per group (**Figure 12**).

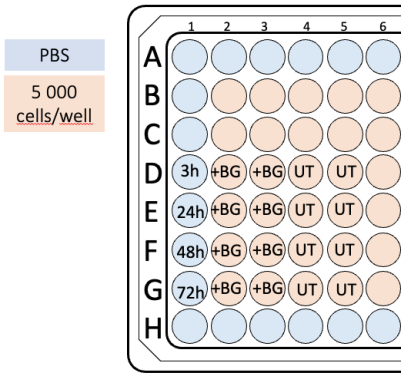

***Figure 12**: **Scheme of 96-well plate for BG-treatment** at different timepoints, as indicated. BG = Bacterial Ghost, UT = untreated*

On day 14, 20 µL of medium was removed from wells D2-D5, followed by the removal of 10 µL from the remaining wells in rows E to G. For all treated wells (labelled as "+BG"), 10 µL of AF488 labelled BG solution containing $1x10^7$ BGs (in PBS) were added. Untreated (UT) wells received 10 µL of PBS, serving as the negative control. The spheroids were incubated for defined time intervals to assess the effects of BG treatment over time, specifically at 3-, 24-, 48- and 72-hours post-treatment.

Two hours before each imaging session, 10 µL of Hoechst solution was added to counterstain cell nuclei with the preparation described in Section 6.4.1. After incubation, the spheroids were washed with PBS and imaged with the FLM equipped with FITC and DAPI filters. The FITC filter was used to visualize BGs, while DAPI filter was used to image cell nuclei stained with Hoechst. Live images were captured using a z-stack ranging from -400 to + 400 µm with a step size of 10 µm. The settings of the microscope and the post-process of the images were conducted according to **Table 9**.

Microscope filter	Exposure Time (ms)	Gain	Threshold
DAPI	20	4	500-5000
FITC	20	4	500-16383

***Table 9**: Settings of the FLM for imaging of CT26Luc spheroids treated with BGs using DAPI and FITC filters, including exposure time, gain and threshold for the post-processing of the images.*

After live imaging, the spheroids were embedded in Tissue-Tek® and sectioned following the procedure outlined in Chapter 6.1.3.1. To investigate the impact of BG treatment on

the TLR4 signalling pathway, IHC staining was performed following the protocol described in Chapter 6.1.3.2. For this purpose, six different primary ABs targeting specific components of the pathway were used, shown in **Table 10**.

Primary AB	Concentration	Localisation
TLR4	6 µg/mL	Membrane
TRAM	4 µg/mL	Cytoplasm
pNFκB	8 µg/mL	Nucleus
IL-6	3.5 µg/mL	Cytoplasm
IL-10	5 µg/mL	Cytoplasm
Ki-67	0.31 µg/mL	Nucleus

Table 10: *Primary ABs used for IHC staining with the corresponding concentration and localisation within the cells.*

The rabbit IgG isotype control was used at two different concentrations (8 µg/mL and 0.4 µg/mL), with the lower-concentrated one applied in the case of Ki-67 to enable longer exposure times, as the AB showed weak staining. For visualization of the primary ABs, the yellow, fluorescent secondary AB NanoSec® 568 (0.5 µg/mL) or the red fluorescent NanoSec® 647 (0.5 µg/mL) was used. The detailed preparation of these solutions is described in Section 6.4.2 with the corresponding excitation and emission maxima shown in **Table 11**.

Secondary AB	Excitation	Emission
NanoSec® 568	578 nm	603 nm
NanoSec® 647	650 nm	665 nm

Table 11*: Excitation and Emission maxima of secondary ABs for IHC staining.*

For imaging, the FLM IX73 equipped with DAPI, FITC and CY3 filters was used. Images were taken at 20x- and 60x-magnifications with the selected exposure times for each filter and edited colour intensities shown in the following tables (**Table 12**, **Table 13**).

Set 1				
Objective	20x		60x	
	Exposure	Threshold	Exposure	Threshold
DAPI	100 ms	1000 - 5000	5 ms	1000 - 14000
FITC	100 ms	0 – 12000 / 500 - 16383	10 ms	1000 - 16383
CY3 (higher-concentrated)	100 ms	500 – 12000	10 ms	1000 - 16383
CY3 (lower-concentrated)	150 ms	500 - 10000	15 ms	500 - 16383
CY5 (higher-concentrated)	-	-	5 ms	1500 - 16383
CY5 (lower-concentrated)	-	-	10 ms	500 - 16383

***Table 12**: Settings of FLM used for imaging the first set of CT26Luc spheroids treated with BGs, separated by magnifications and including exposure times and threshold of the post-process.*

Set 2				
Objective	20x		60x	
	Exposure	Threshold	Exposure	Threshold
DAPI	100 ms	1000 - 10000	5 ms	1000 - 15000
FITC	100 ms	0 – 12000 / 500 - 16383	10 ms	1000 - 12000
CY3 (higher-concentrated)	100 ms	500 – 12000	15 ms	1000 - 16383
CY3 (lower-concentrated)	150 ms	0 - 10000	20 ms	500 - 16383

***Table 13**: Settings of FLM used for imaging the second set of CT26Luc spheroids treated with BGs, separated by magnifications and including exposure times and threshold of the post-process.*

Several staining attempts were carried out during the experiment. To enhance clarity and comparability, the analysed spheroids were divided into two groups: Set 1 (left spheroid) and Set 2 (right spheroid). The first staining was initially examined using 20x-magnification. As the experiment progressed, it was decided to additionally acquire images at 60x- magnification. However, since the initial staining had already been performed some time before, new slides had to be stained again, but at different timepoints. As a result, the exposure times differed between Set 1 and Set 2. Furthermore, threshold values during image analysis were adjusted individually to match the isotype control of each respective slide, which led to differences in the thresholds.

For the FITC filter images, two distinct threshold values are listed in the table: in treated spheroids, the threshold was optimized to enhance BG visibility, while in untreated spheroids, only background noise was removed.

At the end of the experiment, an attempt was made to use red fluorescence instead of the previously applied yellow fluorescence to better visualize the BGs using NanoSec® 647 (0.5 µg/mL). This adjustment was only implemented in Set 1 using 60x-magnification. Consequently, the table for Set 1 also includes the CY5 filter, which required a different exposure time compared to the previously used CY3 filter.

6.4 Materials

6.4.1 List of Solutions

Complete medium

- 450 mL cell culture medium (depending on cell line)
- 50 mL FCS
- 5 mL P/S
- 5 mL L-Glutamine

Resazurin 0.1 mg/mL

- stock: 5 mg RSZ + 5 mL PBS
- 0.1 mg/mL: 0.5 mL stock + 4.5 mL PBS

Hoechst 320 µg/mL | 160 µg/mL

- For necrotic core: 3.2 µL Hoechst + 96.8 µL PBS
- For BG treatment: 1.6 µL Hoechst + 98.4 µL PBS

Propidium iodide 500 µg/mL

- 50 µL stock solution of PI (1 mg/mL)
- 50 µL PBS

Gelatine, 2 % (sterilised through autoclavation)

- 2 g/mL bovine gelatine
- 98 g/mL MiliQ water

Collagen, 6 µg/mL

- 6 µL collagen from calf skin (1 mg/mL)
- 994 µL cold, complete DMEM F-12 Ham medium without phenol red

PFA 4 %

- Hepes buffered saline:
    - 20 mM HEPES (Lot#7E011523 PanReac) ➔ 19.056 g for 4 L
    - 150 mM NaCl (REF: P0293) ➔ 35.064 g for 4 L
    - MiliQ-Water
    - NaOH for adjusting pH to 7.4
- 4 % Paraformaldehyde BioChemica (Lot#4V008654 PanReac) ➔ 160 g for 4 L

DAPI (1:1000)

- 1 µL DAPI staining solution 1 mg/mL
- 999 µL PBS

Isotype Controls

- 8 µg/mL: 0.8 µL Rabbit IgG isotype control (5 mg/mL) + 499.2 µL BB
- 0.4 µg/mL: 40 µL from the first isotype control + 360 µL BB

Primary ABs

- TLR4 (1:100): 2 µL AB + 198 µL BB
- TRAM (1:100): 2 µL AB + 198 µL BB
- pNFκB (1:100): 2 µL AB + 198 µL BB
- IL-6 (1:200): 1 µL AB + 199 µL BB
- IL-10 (1:200): 1 µL AB + 199 µL BB
- Ki-67 (1:100): 2 µL AB + 198 µL BB

Secondary ABs (1:1000)

- 1 µL Alexa Fluor® 568 anti-rabbit IgG or Alexa Fluor® 647 anti-rabbit IgG
- 999 µL BB

6.4.2 List of Antibodies

- Rabbit IgG isotype control, ThermoScientific, REF: 02-6102, Lot#XK366556
- TLR4 polyclonal antibody, proteintech, REF: 19811-1-AP, Lot#00137395
- TRAM1 rabbit polyclonal antibody, proteintech, REF: 12705-1-AP, Lot#00038803
- pNFκB p65 [Ser529] polyclonal antibody, invitrogen, REF: 44-711G, Lot#2941809
- IL-6 rabbit polyclonal antibody, proteintech, REF: 26404-1-AP, Lot#00136001
- IL-10 recombinant antibody, proteintech, REF: 82191-3-RR, Lot#23009027
- Ki-67 recombinant rabbit monoclonal antibody, invitrogen, REF: MA5-14520, Lot#ZG4390031
- Nano-Secondary® anti-rabbit IgG recombinant antibody VHH Alexa Fluor® 568, chromotek, REF: srbAF568-1-10, Lot#90222043F3
- alpaca anti-rabbit IgG recombinant VHH Alexa Fluor® 647, chromotek, REF: srbAF647-1-5, Lot# 90225043AF2

6.4.3 List of Cell Lines

- CT26Luc
- EEC 12Z
- HT29

6.4.4 List of Materials, Reagents and Devices

- Advanced PAP Pen, Sigma-Aldrich, REF: Z672548
- Cell culture flask T75, Sarstedt, REF: 83.3911.002
- Cell culture medium:
    - DMEM F-12 Ham, Sigma-Aldrich, REF: D6421 (CT26Luc)
    - DMEM F-12 w/o phenol red, Gibco, REF: 21041-025 (EEC12Z)
    - McCoy's 5A, Sigma-Aldrich, REF: M8403 (HT29)
- Collagen from calf skin, Sigma-Aldrich, REF: C8919
- Counting chamber, 0.0025 mm^2, 0.1 mm depth, Marienfeld Brand, REF: 718005
- Coverslips, 24 x 50 mm, Epredia, REF: BB02400500A113MNZ0
- CT15 Tube, Sarstedt, REF: 62.554.502
- CT50 Tube, Sarstedt, REF: 62.548.004
- DAPI solution (1 mg/mL), Sigma-Aldrich, REF: D9542
- Disposable base mold, EMS, REF: 62352-07
- Dulbecco's phosphate buffered saline, Sigma-Aldrich, REF: D8537
- Foetal calf serum, heat inactivated, BioWest, REF: S181H-500
- Hoechst (bis-Benzimide H-33342), Thermo Fisher, REF: J62134
- Injekt® Luer Solo, 10 mL, Braun, REF: 4606108V
- Kimtech®, 11 x 21, Kimberley-Clark Professional, REF: 7552
- L-Glutamine 200 mM solution, Sigma-Aldrich, REF: G7513

- Microscope IX73, Olympus
    - DP-73 colour camera, Olympus
    - Objectives:
        - 10x, UPLFLN10X2/0.30, Olympus
        - 10x, CPLN10xPH/0.25, Olympus
        - 20x, LCACH20XPH/0.45, Olympus
        - 60x, PLAPON60XO/0.42, Olympus
- Nunclon™ delta surface, flat 96 well plate, ThermoScientific, REF: 167008
- Penicillin-Streptomycin, Sigma-Aldrich, REF: P0781
- Propidium iodide solution, Sigma-Aldrich, REF: P4864
- Resazurin powder, ThermoScientific, REF: 418900050
- Serological pipettes, 5 mL, Sarstedt, REF: 86.1253.001
- Serological pipettes, 10 mL, Sarstedt, REF: 86.1254.001
- Serological pipettes, 25 mL, Sarstedt, REF: 86.1685.001
- SmartBlock™, 10 mL, Lot# 113E040r
- Superfrost™ microscope slides, Epredia, REF: AA00008032E01MNZ10
- Superfrost Plus™ adhesion microscope slides, Epredia, REF: J1800AMNZ
- Syringe filter, PES 0.2 µm, fisherbrand, REF: 15206869
- TC-plate 96 well, BIOFLOAT™, round bottom, Sarstedt, REF: 83.3925.400
- Tecan® plate reader infinite M200PRO
- Tissue-Tek® O.C.T compound, Sakura, REF: 4583
- Triton-X-100, Sigma-Aldrich, Lot# SLBM3864V
- TrypLE express enzyme w/o phenol red, Gibco, REF: 12604021
- Vectashield® Antifade mounting medium, Vector Laboratories, REF: H1900

7 RESULTS AND DISCUSSION

In this chapter the data obtained from spheroid formation, cell viability assays and necrotic core formation as well as the BG treatment studies on TLR4 pathway are presented and critically interpreted.

7.1 Optimization of Spheroid Formation

This section presents the results to optimize the spheroid formation in HT29 and EEC 12Z cell lines, including PH images, RSZ assays and the necrotic core formation as well as the supplementation of gelatine and collagen.

7.1.1 HT29 Spheroids

The aim of these experiments is to optimize spheroid formation of HT29 cells. Various experimental procedures were applied based on morphological characteristics and growth patterns. Cells were seeded with different cell amounts to assess the cell viability via RSZ assays and to evaluate the necrotic core via Live/Dead staining. The exact steps of the workflow can be found in Chapter 6.2.1.

Figure 13 presents PhC images confirming the successful formation of spheroids. Throughout the experiment, the spheroids exhibit substantial growth, with a noticeable increase in size. Most of the structures maintain a well-defined, spherical morphology and appear densely packed. In some instances, fibrous material can be detected within the wells, adhering to the cells and subsequently integrating into the spheroid architecture. Notably, the outer edges of the spheroids appear irregular and lack a clearly defined border. At around day 10, for some spheroids (especially seen in well number D2 and F5) a coronal layer of dead cells becomes apparent, likely resulting from mechanical stress and nutrient limitations at the periphery. As no significant visually difference in size is detected, a seeding number of 5k cells per well was chosen for further experiments. The results indicate that the growth pattern and morphology of the spheroids remain consistent, demonstrating reproducibility of spheroid formation under the given conditions.

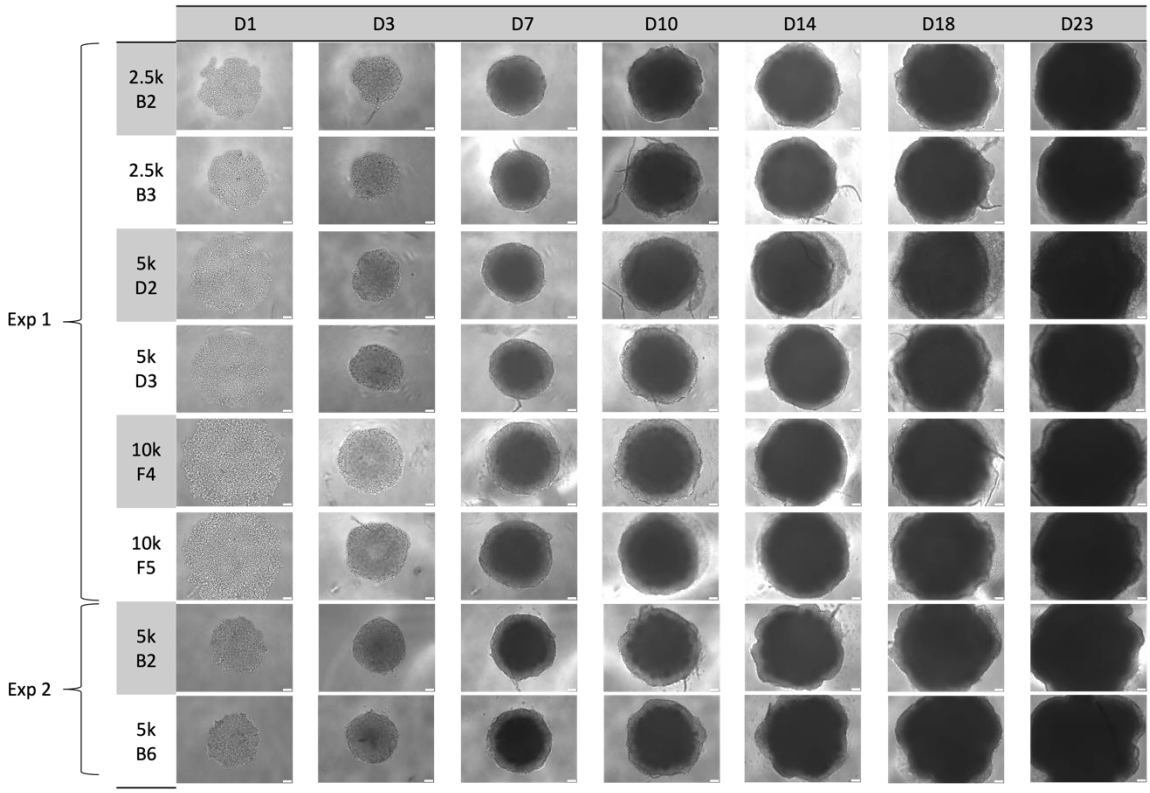

***Figure 13**: **Phase Contrast pictures of HT29** spheroids with three different seeding numbers (2.5k, 5k, 10k) at different timepoints, as indicated. Two replicates (labelled with well numbers) are shown from n = 5 spheroids. Pictures taken with 10x-magnification with an exposure time of 10 ms. Bar size: 100 µm. D = Day, Exp = Experiment, k = thousand*

Spheroid viability during the cultivation period of the two experiments is presented in **Figure 14**. A common trend observable in both datasets is a steady increase in relative fluorescence units (RFU), with a notable rise between day 14 and day 18, followed by a slight decline after day 18.

However, there are key differences in the measured data between the two experimental runs. In the first experiment, the initial RFU are lower compared to the second experiment. Additionally, the peak RFU are higher across all cell densities, ranging between 12.000 and 15.000, whereas in the second experiment, the maximum RFU only reach approximately 8.000.

Several factors may explain these discrepancies. Since the RSZ solution was prepared manually for each read-out, variations in concentration and preparation could contribute to the differences in absolute RFU. Additionally, the second experiment was conducted at a later timepoint, by which the handling abilities might have improved. This

may have influenced the accuracy of pipetting and led to slight variations in actual well volumes, which can affect the RSZ assay results. For better standardization, a repeat experiment would be beneficial to reduce variability and determine true RFU, which are likely to fall somewhere between the two experimental outcomes. Nevertheless, both experiments demonstrated a consistent pattern of metabolic activity, confirming that spheroids with a higher initial cell density tend to exhibit higher RFU. However, this difference is not significant, considering that twice the number of cells were seeded, but the RFU is not twice as high.

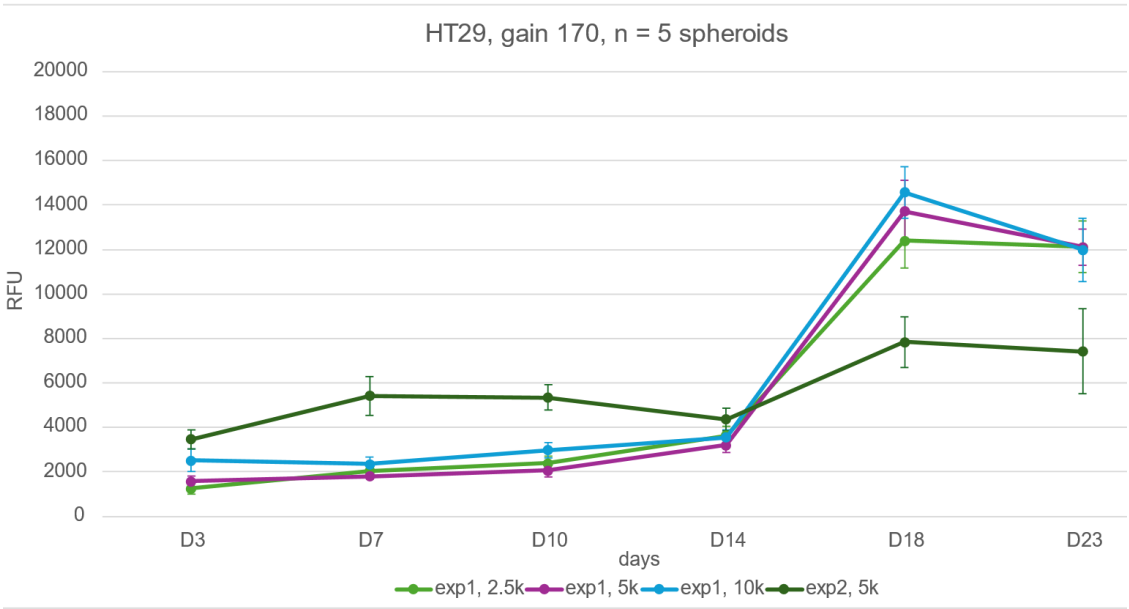

***Figure 14**: **Results of Resazurin Assays** of Experiment 1 and Experiment 2, conducted over 23 days of HT29 spheroids with initial seeding number of 2.5k, 5k and 10k (Exp 1) and only 5k (Exp 2). RFU = relative fluorescence units; average of n=5 spheroids, k = thousand*

To finalize the HT29 spheroid characterization, necrotic core formation was evaluated with a Live/Dead staining using two replicates per seeding number to distinguish non-viable from viable cells. Spheroids were imaged using a FLM with a z-stack acquisition as described in Section 6.1.2.3.

The results of the Live/Dead staining assay, presented in **Figure 15**, illustrate the progressive formation of the necrotic core within the spheroids. During the first week in culture, only a few isolated dead cells are visible, indicating that cell death is initially minimal. However, after one week in culture a significant increase in necrotic cells can

be observed, with the necrotic core becoming highly pronounced. After two weeks, the proportion of dead cells surpass that of viable cells, leading to a loss of structural definition within the spheroid. The yellow fluorescence signal, indicative of non-viable cells, becomes predominant, making it difficult to clearly distinguish the boundaries of the necrotic core. This suggests that extensive cell death and progressive loss of viability occurs over time. The appendix includes a figure illustrating each layer of one spheroid per seeding number (**Figure 33A**).

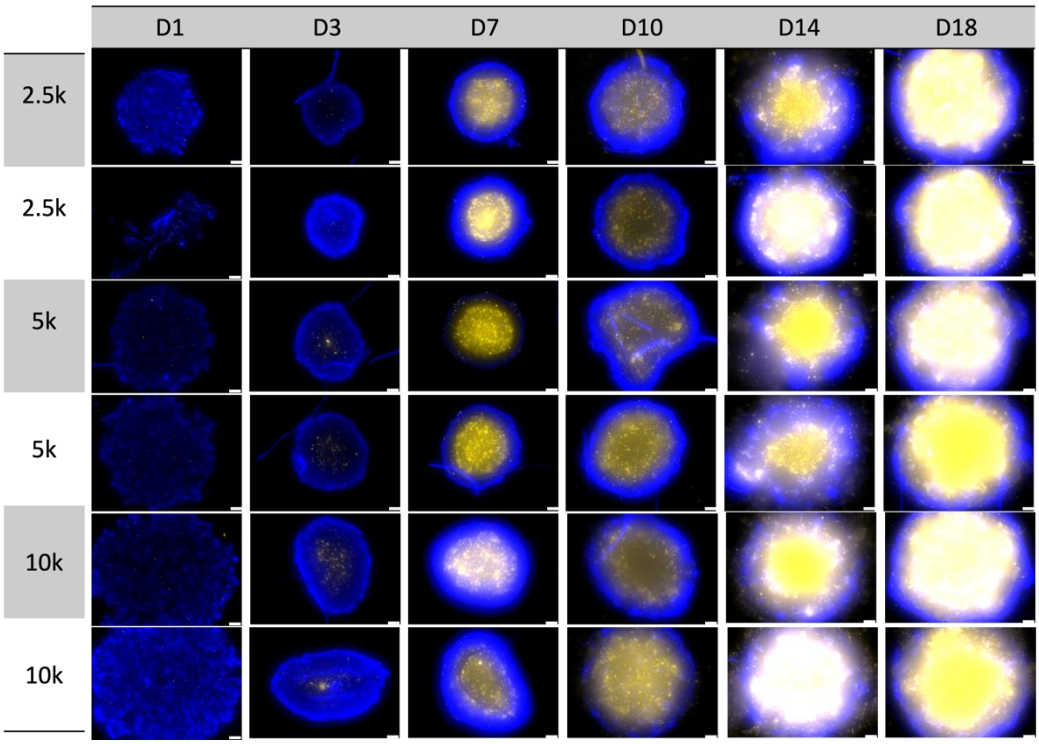

***Figure 15**: **Necrotic core formation of HT29** spheroids imaged by fluorescence microscope. Blue = Hoechst (conc. 320 µg/mL, exposure time = 40 ms) with DAPI filter, Yellow = PI (conc. 500 µg/mL, exposure time = 10 ms) with CY3 filter. 2 h incubation for staining solutions. D = Day, k = thousand*

7.1.2 EEC 12Z Spheroids

The aim of this experiment is to optimize spheroid characterization of EEC 12Z cells. The same experimental procedures, as for HT29, were applied based on morphological characteristics and growth patterns. The exact steps of the workflow can be found in Chapter 6.2.2.

PhC microscopy images presented in **Figure 16** confirm the successful formation of spheroids at progressing time points. The generated spheroids exhibit a compact and spherical morphology, although some irregularities in structure can be observed due to the presence of fibres in the 96-well plate. The spheroids are smaller in size but display a defined boundary without developing a coronal layer. Based on the PhC images, no distinct increase in size can be recognised visually from day 3 onwards. It appears that the spheroids have a similar size, regardless of the initial seeding number.

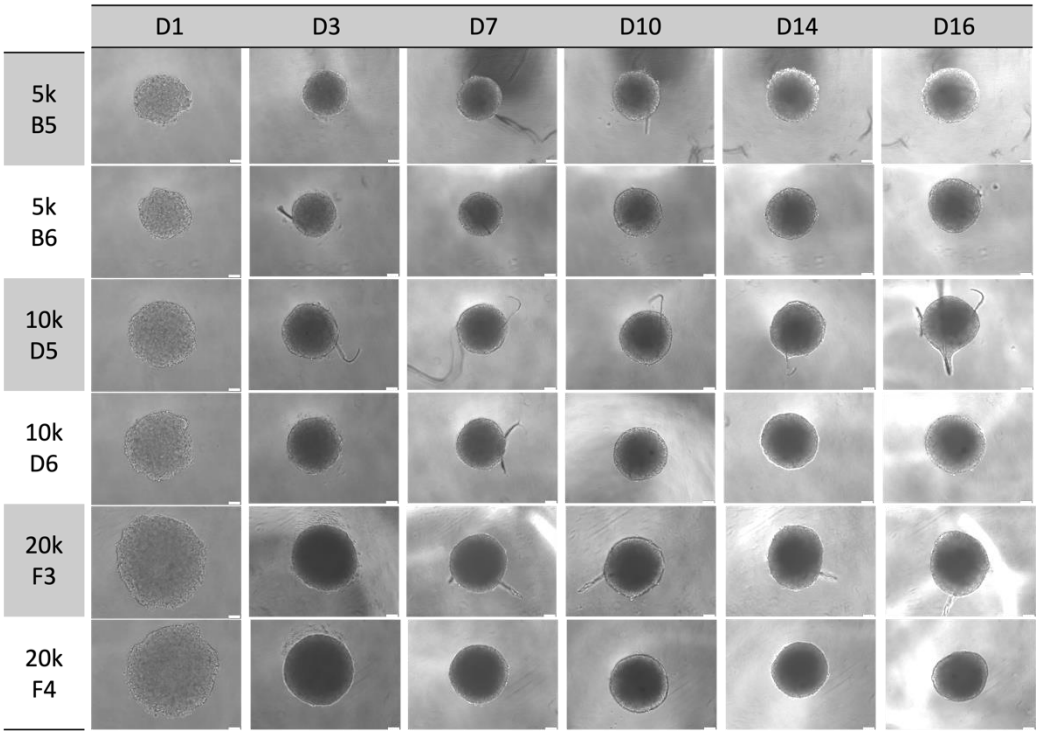

***Figure 16**: **Phase Contrast pictures of EEC 12Z** spheroids with three different seeding numbers (5k, 10k, 20k) at different timepoints, as indicated. Two replicates (labelled with well numbers) are shown from n = 5 spheroids. Pictures taken with 10x-magnification with an exposure time of 10 ms. Bar size: 100 µm. D = Day, k = thousand*

For analysing the cell viability, multiple RSZ assays were conducted, with the results presented in **Figure 17**. These results demonstrate a continuous increase in RFU throughout the entire experimental period, except for spheroids seeded at 20k cells, which exhibit a decline between day 10 and day 14. Notably, by the final measurement point, spheroids seeded with 10k cells per well surpass those seeded with 20k cells per well in RFU. However, the standard deviation for this data point was relatively high, suggesting potential variability. This could indicate that the actual RFU may be lower than recorded confirming that spheroids with a higher cell count per well achieve a higher RFU.

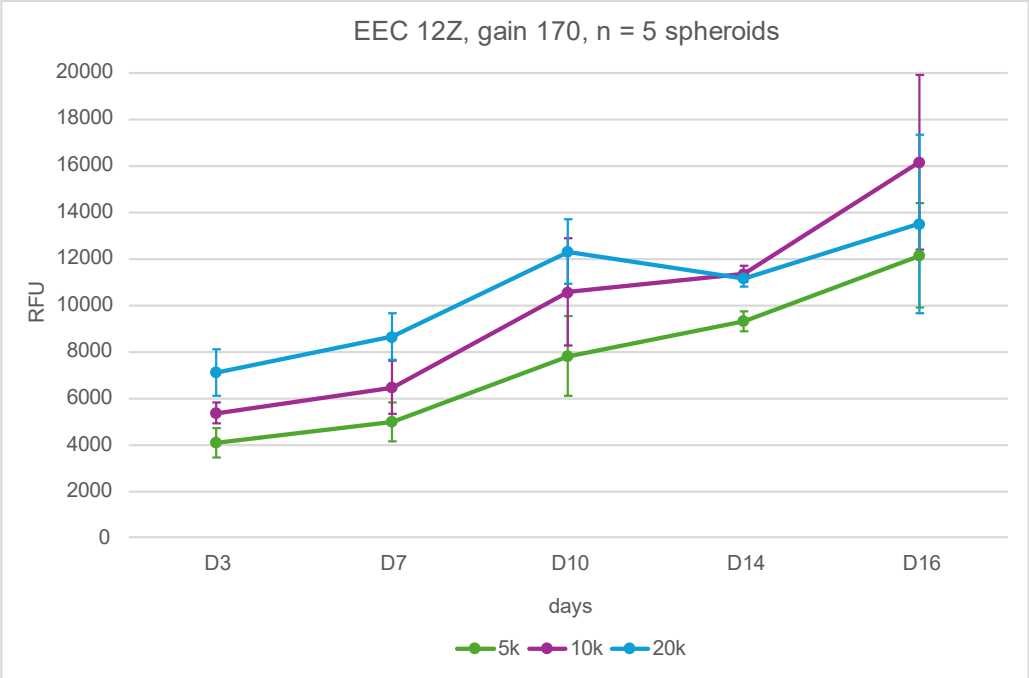

Figure 17: ***Results of Resazurin Assays****, conducted over 16 days of EEC 12Z spheroids with initial seeding number of 5k, 10k and 20k. RFU = relative fluorescence units; average of n=5 spheroids, k = thousand*

For the evaluation of the necrotic core, the same procedure as for HT29 spheroids was used, with the workflow described in Chapter 6.1.2.3

Figure 18 presents the results of the Live/Dead staining performed on EEC 12Z spheroids, revealing the early onset of necrotic core formation. 24 hours after seseding (day 1) a few non-viable cells are already detectable within the spheroids. By day 3, the necrotic core is clearly distinguishable, indicating a rapid progression of cell death in the inner regions probably due to insufficient nutrient supply. After one week, the necrotic core becomes the dominant feature within the spheroid. However, in EEC 12Z spheroids it remains relatively stable for the residual timepoints of the experiment. A sharp boundary between viable and non-viable cells persists, suggesting that cell death progression plateaus after the initial phase. Additionally, the appendix includes a figure presenting each layer of a single spheroid per cell density (**Figure 34A**).

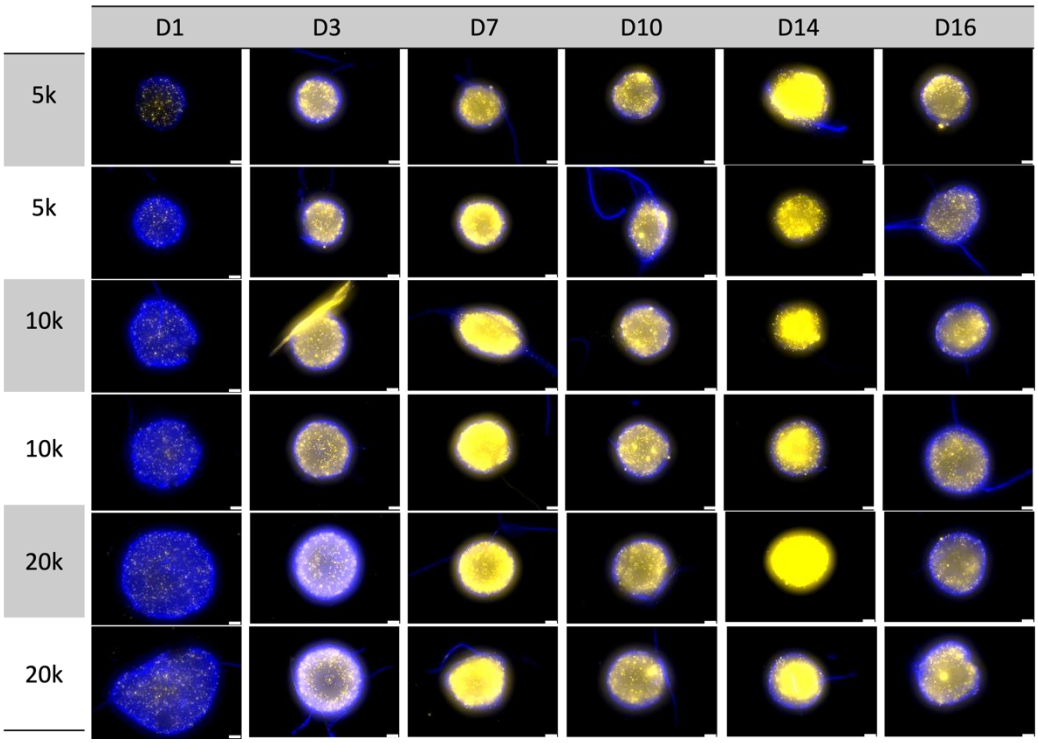

***Figure 18**: **Necrotic core formation of EEC 12Z** spheroids imaged by fluorescence microscope. Blue = Hoechst (conc. 320 µg/mL, exposure time = 40 ms) with DAPI filter, Yellow = PI (conc. 500 µg/mL, exposure time = 10 ms) with CY3 filter. 2h incubation for staining solutions. D = Day, k = thousand*

As demonstrated by the results, EEC 12Z cells form spheroids successfully. However, their small size leads to significant challenges during cell culture handling. To address this issue and optimize spheroid formation, an additional experiment was conducted to evaluate whether the supplementation of gelatine and collagen could influence spheroid size and cell viability. The working steps were conducted according to Chapter 6.2.2.

Figure 19 shows PhC microscopy images of EEC 12Z spheroids captured at different timepoints. Images show that the spheroids maintain a consistent size over time, suggesting that neither gelatine nor collagen supplementation have a significant impact on their overall growth. The spheroids retain a well-defined structure, especially the collagen-treated ones. Untreated spheroids and spheroids treated with gelatine exhibit a slightly irregular shape compared to the collagen-treated ones after two weeks. However, this morphological variation could also be caused by the presence of fibrous material within the wells or by accidental pipetting of the spheroid.

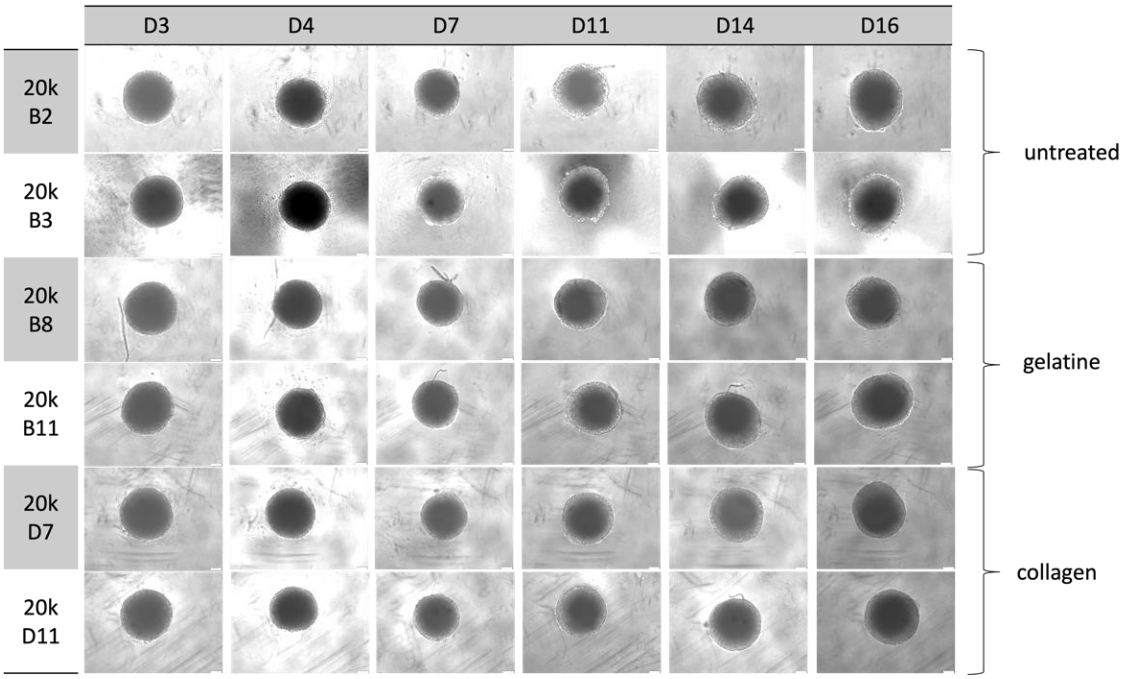

***Figure 19**: **Phase Contrast pictures of EEC 12Z** spheroids with an initial seeding number of 20k cells per well at different timepoints, as indicated. Upper row: untreated, middle row: treated with gelatine, lower row: treated with collagen. Two replicates (labelled with well numbers) are shown from n = 5 spheroids. Pictures taken with 10x-magnification with an exposure time of 10 ms. Bar size: 100 µm. D = Day, k = thousand*

To evaluate cell viability and growth dynamics, RSZ assays were performed at multiple timepoints. The results, presented in **Figure 20**, reveal that spheroids treated with collagen exhibit the highest RFU, followed by the untreated spheroids, whereas gelatine-treated spheroids showed the lowest metabolic activity. However, this is not significantly lower, as the standard deviations still overlap.

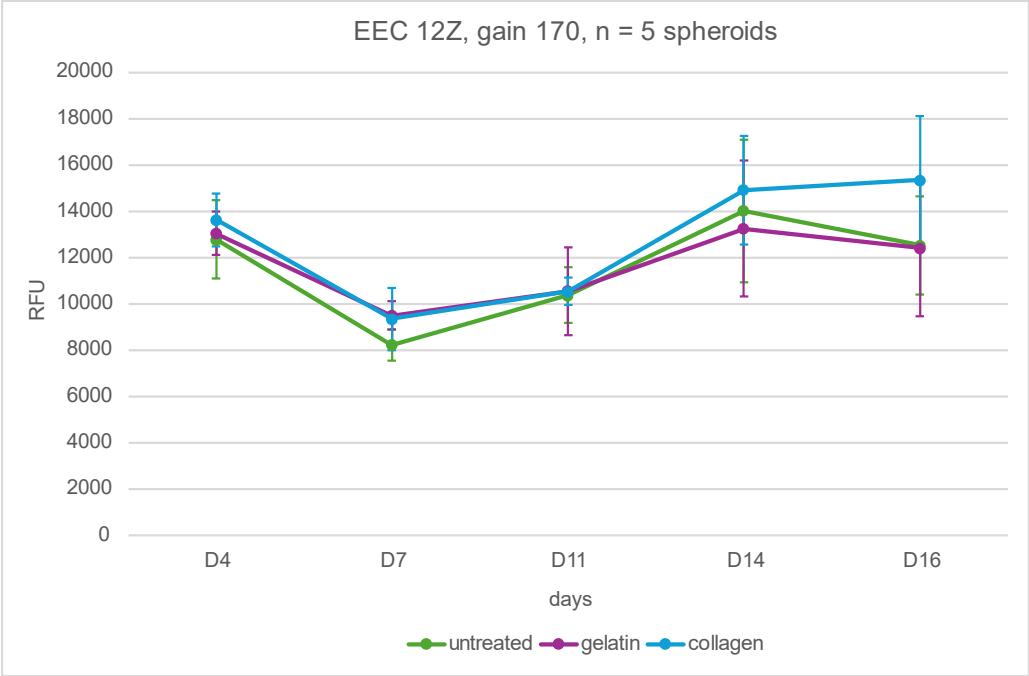

***Figure 20**: **Results of Resazurin Assays**, conducted over 16 days of EEC 12Z spheroids with initial seeding number of 20k. Difference between untreated spheroids and treated spheroids with gelatine or collagen. RFU = relative fluorescence units; average of n=5 spheroids*

By day 16, collagen-treated spheroids reach their peak of approximately 15.000 RFU, whereas both untreated and gelatine-treated spheroids displayed similar RFU, plateauing at around 12.000. This indicates that collagen supplementation leads to a moderate increase in cellular metabolic activity, suggesting a potential enhancement in spheroid growth or viability.

When comparing these findings to those of the previous experiment, it becomes evident that collagen supplementation results in a slight increase in spheroid size. However, this size difference was not visually distinguishable under PhC microscopy and was only detectable through RSZ assay measurements. Further investigations are needed to determine whether collagen-induced metabolic activity translates into long-term structural or functional changes in EEC 12Z spheroids.

7.2 Influence of BG-Treatment on CT26Luc Spheroids

The objective of this project is to implement BGs into CT26Luc spheroids with a cell density of 5k cells per well and subsequently perform IHC staining to visualize the TLR4 signalling pathway. The detailed workflow is described in Chapter 6.3.

Figure 21 presents a compilation of PhC images taken at different timepoints, illustrating the growth dynamics of CT26Luc spheroids. Over time, the spheroids exhibit increasing growth and a well-defined outer boundary without a coronal layer, indicative of compactness. While most spheroids display uniform morphology and size, some variability is observed, particularly in well B8, where fibrous material within the well altered spheroid architecture.

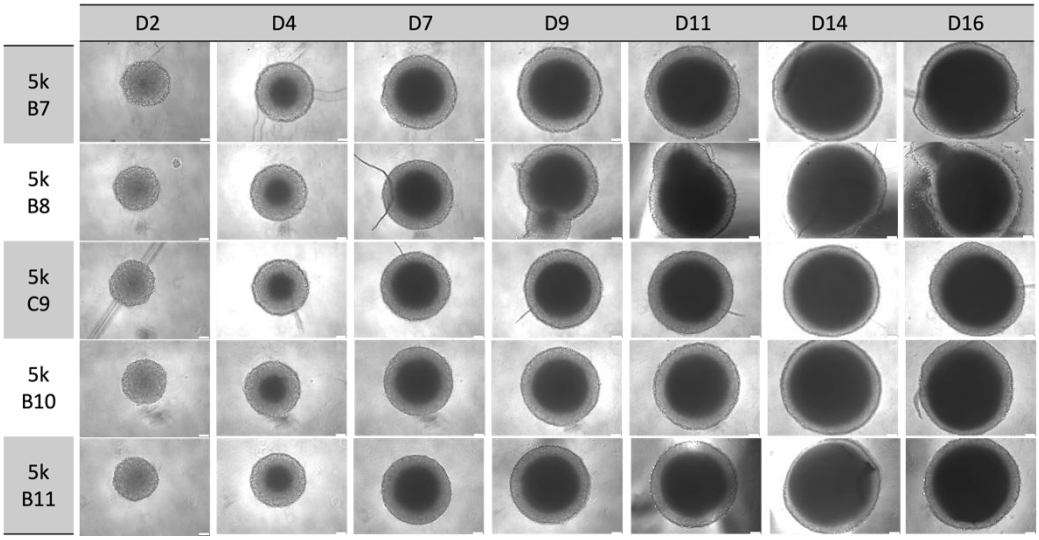

Figure 21: Phase Contrast pictures of CT26Luc *spheroids with an initial seeding number of 5k at different timepoints, as indicated. Five replicates (labelled with well numbers) are shown over seven timepoints (n = 5). Pictures were taken with 10-x magnification with an exposure time of 10 ms. Bar size: 100 µm. D = Day, k = thousand*

The results of the RSZ assays are presented in **Figure 22**. A total of seven assays were conducted over a 16-day period to assess cell viability. The data indicates a continuous increase in spheroid growth throughout the experiment, with a notable rise in RFU from day 9 onwards, reaching a peak of approximately 15.000 RFU. Exceptionally, after day 7 and day 11, a slight decrease is observed, possibly due to differences in RSZ-preparation, nutrient depletion or the onset of necrotic core formation within the spheroids.

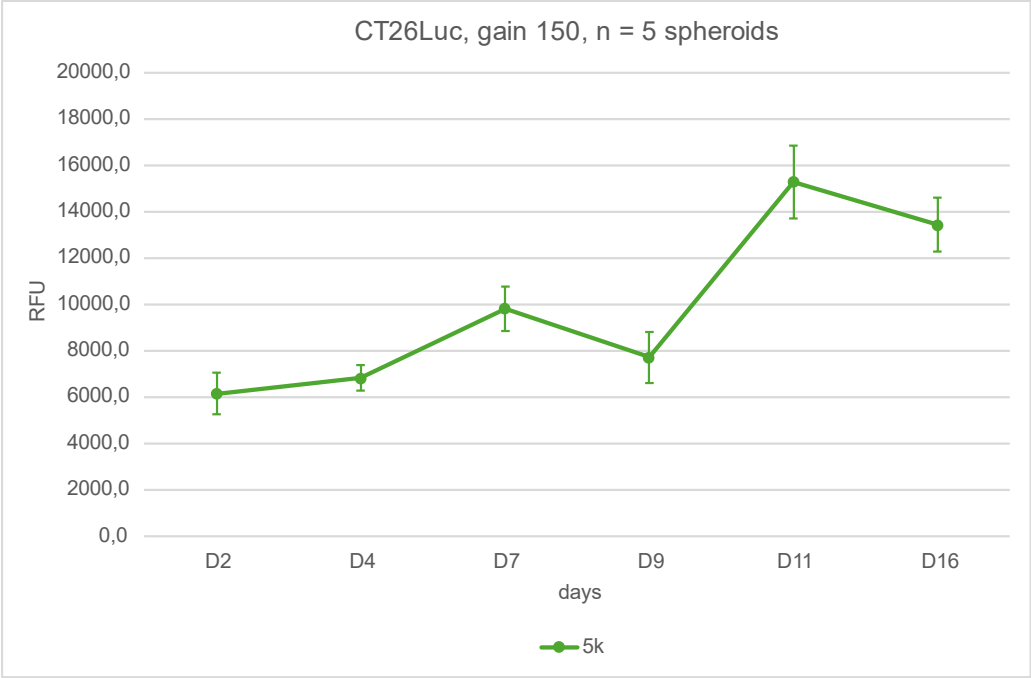

Figure 22: ***Results of Resazurin Assays****, conducted over 16 days of CT26Luc spheroids with initial seeding number of 5k. RFU = relative fluorescence units; average of n=5 spheroids, k = thousand*

Figure 23 presents the results of CT26Luc spheroids treated with BG AF488 at different timepoints. For each timepoint, two spheroids treated with BGs were analysed, while two spheroids treated with the same amount of PBS served as untreated controls.

The results clearly show that as early as 3 hours post-incubation, some BGs are already associated or entered the spheroids. The number of integrated BGs increase progressively with longer incubation times. In contrast, no BGs are detected in the untreated control spheroids, except for a single instance in spheroid one of the 48-hour incubation group. This unexpected fluorescence signal is likely the result of accidental BG transfer, possibly caused by pipette tip contamination during sample handling.

For better visualization, an overlay of FITC and DAPI filters is provided in the upper row, while the lower row displays FITC-only images, highlighting the distribution of BGs within the spheroids. These images were acquired using Z-stack imaging, spanning a range of -400 to +400 µm, with a step size of 10 µm, meaning that layer-by-layer images were captured and subsequently reconstructed into a composite image. This should be considered when interpreting the fluorescence intensity and BG localization.

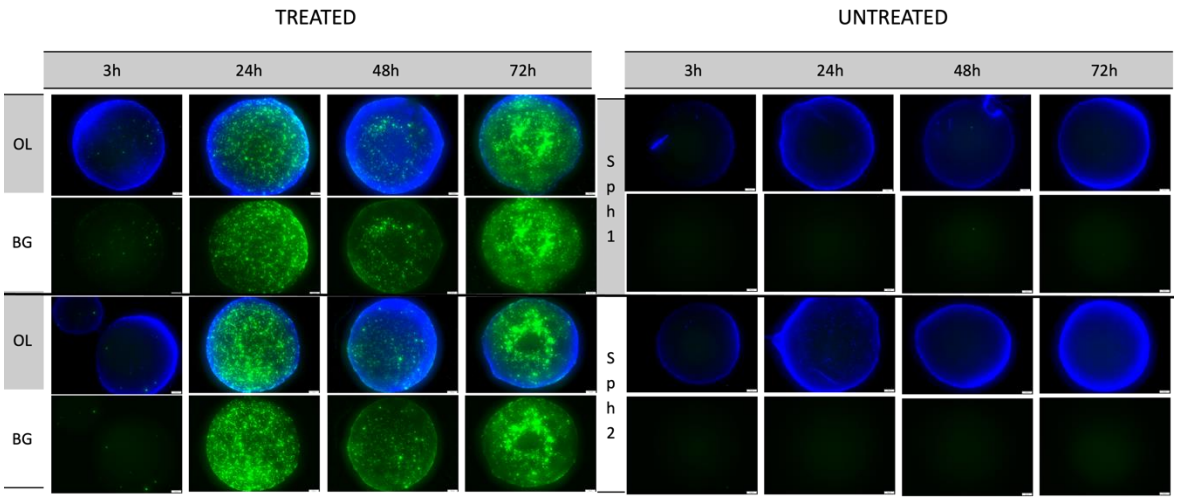

***Figure 23*:Results of CT26Luc spheroids treated with BGs** *at 3h, 24h, 48h and 72h post-exposure (left) and untreated (right) of two spheroids each. Green = AF488-BGs (conc. 1x10^7 BGs/10 µL, exposure time = 20 ms) with FITC filter. Blue = Hoechst (conc. 160 µg/mL, exposure time = 20 ms) with DAPI filter. Microscope settings: z-stack ranging from -400 to + 400 µm with a step size of 10 µm, gain of 4. BG = bacterial ghost, OL = Overlay. Bar size = 100 µm.*

Due to the overlay of the single layers, the impression is created that the BGs are evenly distributed over the entire spheroid. However, BGs show a preferential accumulation in the outer zone without moving to the centre of the spheroid. This is illustrated by **Figure 24**, which shows sectioned spheroids to better represent the actual localisation of the BGs within the spheroid.

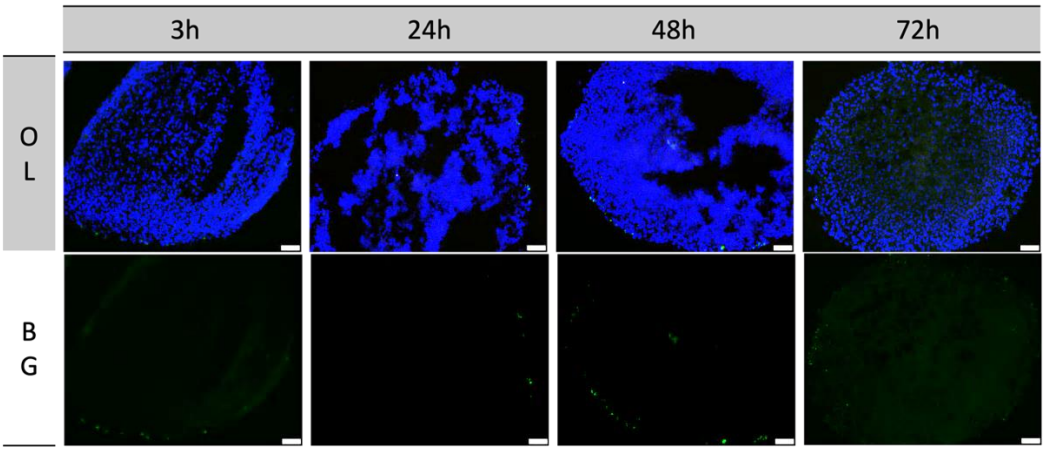

Figure 24: Distribution of BGs *within the spheroid. Pictures presenting sectioned spheroids at different timepoints, as indicated. The upper row shows an overlay of DAPI and FITC whereas the lower row shows only FITC-taken images to represent the actual localisation of the BGs. Bar size = 50 µm*

Overall, the results demonstrate that BG treatment of CT26Luc spheroids is successful, with an increasing accumulation of BGs within the spheroids architecture over the incubation period. However, they only stay in the outer zone and can't reach the inner core of the spheroid. After embedding and sectioning the spheroids, IHC staining was performed with the detailed workflow described in Section 6.3. The following figures illustrate the stained parts of the TLR4 signalling pathway, shown in Chapter 4.4.

For the sake of consistency and clarity, only the spheroids from Set 1 are presented in the result section. To avoid confusion in colour interpretation, images acquired with red fluorescence secondary AB were post-processed to appear yellow, ensuring a uniform visual presentation. The corresponding images from Set 2 are provided in the appendix (**Figure 39A**-**Figure 42A**).

To provide a brief overview of the 20x-magnification results, two representative figures are presented from an early timepoint (3 h) and from a later timepoint (72 h) with the other two incubation periods shown in the appendix (**Figure 35A**, **Figure 36A**). As displayed in **Figure 25**, only a few BG signals are visible after a 3-hour incubation period. This can be attributed to the fact that the spheroids were sectioned, and overall, only limited BG presence can be observed in the overlay. Consequently, the signals from the primary ABs remain weak at this stage. Nevertheless, a slight staining is already detectable, particularly for pNFκB.

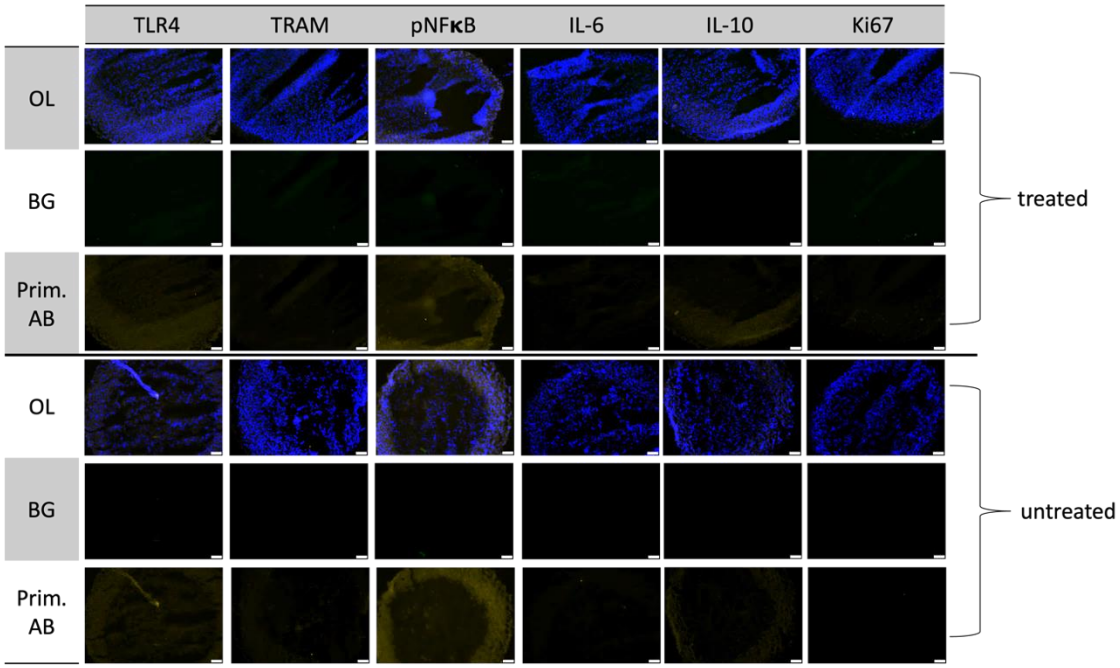

***Figure 25**: **Results of IHC staining – 3h** of CT26Luc spheroids treated with AF488-BGs (upper row) and untreated control groups (lower row) showing one spheroid of n = 2 spheroids using six different primary antibodies visualized with secondary antibody. Images taken with fluorescence microscope at 20x-magnification. Green = AF488-BGs with FITC filter; Blue = Hoechst with DAPI filter; Yellow = secondary AB with CY3 filter. Bar size = 50 µm, OL = Overlay.*

After 72 hours of incubation, a noticeable increase in BG signals is observed, accompanied by stronger signals from the stained primary ABs, as shown in **Figure 26.** Clear differences between treated and untreated group are particularly evident in the TRAM and IL-6 signals, which indicates that BG-treatment leads to their activation.

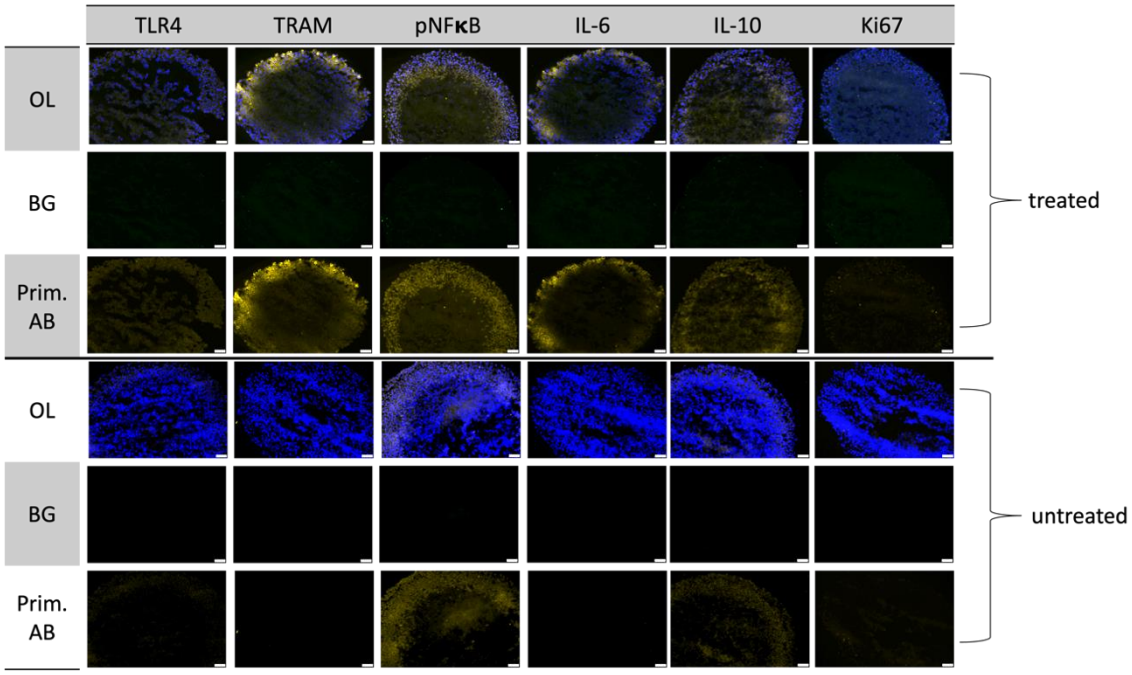

***Figure 26**: **Results of IHC staining – 72h** of CT26Luc spheroids treated with AF488-BGs (upper row) and untreated control groups (lower row) showing one spheroid of n = 2 spheroids using six different primary antibodies visualized with secondary antibody. Images taken with fluorescence microscope at 20x-magnification. Green = AF488-BGs with FITC filter; Blue = Hoechst with DAPI filter; Yellow = secondary AB with CY3 filter. Bar size = 50 µm, OL = Overlay*

To allow a more detailed visualization of the staining patterns, additional imaging was performed at 60x-magnification (with immersion oil), as presented in the following figures with the isotype controls presented in the appendix (**Figure 37A**, **Figure 38A**).

As previously described in Chapter 4.4, the initial step in the TLR4 signalling pathway is the recognition of LPS on the surface of BGs from the TLR4. IHC staining confirmed the presence of TLR4 in CT26Luc spheroids, as shown in **Figure 27**. However, as the signal intensity was similar in both treated and untreated spheroids, it can be concluded that the staining verified the general expression of this transmembrane receptor, rather than its activation. This finding is consistent with the information that TLR4 is ubiquitously present on immune and epithelial cells and that its activation requires complex formation with MD-2 and CD14, but that its presence alone is not enough (Kawai & Akira, 2010).

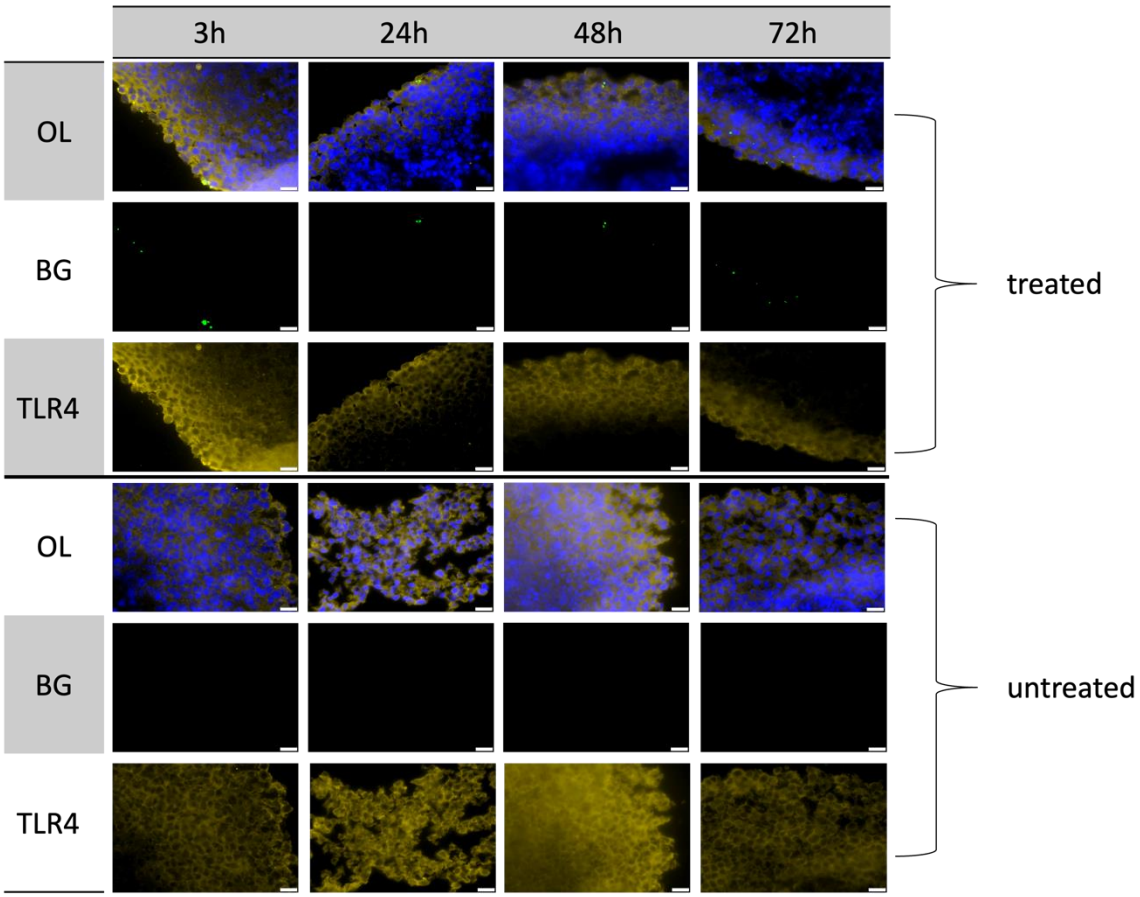

***Figure 27**: **Results of IHC staining – TLR4** of CT26Luc spheroids treated with AF488-BGs (upper row) and untreated control group (lower row), after different incubation periods (3h, 24h, 48h, 72h), showing one spheroid of n = 2 spheroids. Images taken with fluorescence microscope at 60x-magnification. Green = AF488-BGs with FITC filter; Blue = Hoechst with DAPI filter; Yellow = secondary AB-labelled primary AB for TLR4 with CY3 filter. Bar size = 20 µm, OL = Overlay.*

In contrast to TLR4, **Figure 28** reveals a clear difference in TRAM signal intensity between treated and untreated spheroids, with pronounced TRAM signals observed exclusively in the treated group. No signals are seen in the untreated group, except for 3 h and 24 h post-incubation. This observation is presumably the result of an artifact or pronounced background noise that could not be sufficiently removed during image processing. This strongly indicates that BGs activate the TRAM-dependent pathway after TLR4-activation. Interestingly, TRAM localization correlates precisely with BG presence and the signal intensity increases proportionally, suggesting that the intended TRAM-dependent signalling cascade has been successfully triggered by BG-treatment. This result is consistent with previous reports identifying TRAM as a TLR4-specific adapter molecule required for the MyD88-independent cascade (Fitzgerald et al., 2003).

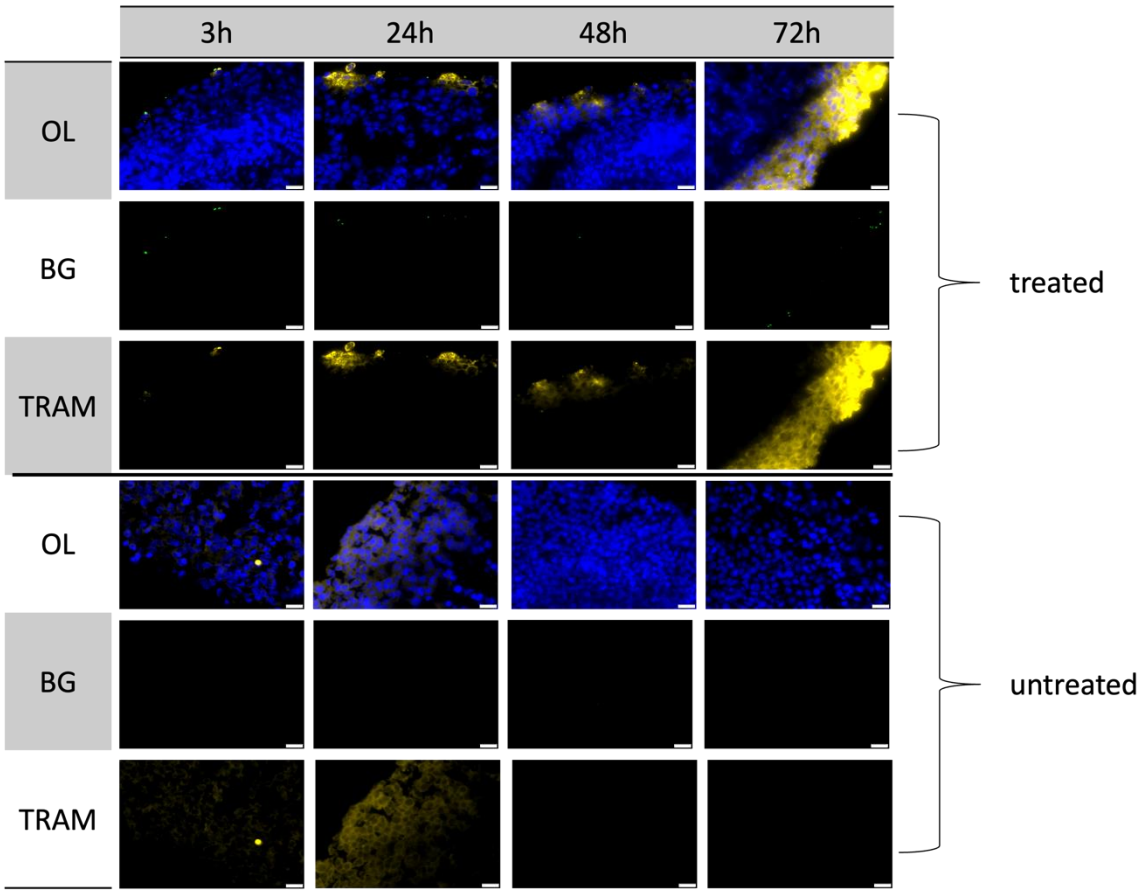

Figure 28: Results of IHC staining – TRAM *of CT26Luc spheroids treated with AF488-BGs (upper row) and untreated control group (lower row), after different incubation periods (3h, 24h, 48h, 72h), showing one spheroid of n = 2 spheroids. Images taken with fluorescence microscope at 60x-magnification. Green = AF488-BGs with FITC filter; Blue = Hoechst with DAPI filter; Yellow = secondary AB-labelled primary AB for TRAM with CY3 filter. Bar size = 20 µm, OL = Overlay.*

The original hypothesis of this experiment was that BGs would lead to activation of NFκB. However, both treated and untreated spheroids exhibit strong signals of pNFκB, as shown in **Figure 29**. This result does not indicate that NFκB activation is not specifically triggered by BG treatment, but rather that the NFκB pathway is permanently active. This has already been observed in various tumour types, including CRC, where NFκB supports cell survival and proliferation as well as immune evasion (Karin & Greten, 2005). This effect can be based on various mechanisms, such as autocrine cytokine loops, mutations or overlaps with parallel oncogenic signalling pathways (Pikarsky et al., 2004).

Moreover, 3D tumour spheroids have been shown to amplify stress- and inflammation-induced signals, possibly triggering sustained NFκB activation that promotes tumour

aggressiveness and resistance to therapy (Bissell & Hines, 2011). For this reason, the observed constitutive expression of pNFκB could be due to the spheroid structure itself, thereby masking the possible inductions by BGs.

However, the lack of differential pNFκB activation in treated spheroids could also suggest that BG treatment does not actually affect this cascade, but rather an alternative TRAM-dependent signalling pathway. This NFκB-independent pathway would also lead to the release of proinflammatory cytokines such as IL-6 (Fitzgerald et al., 2003).

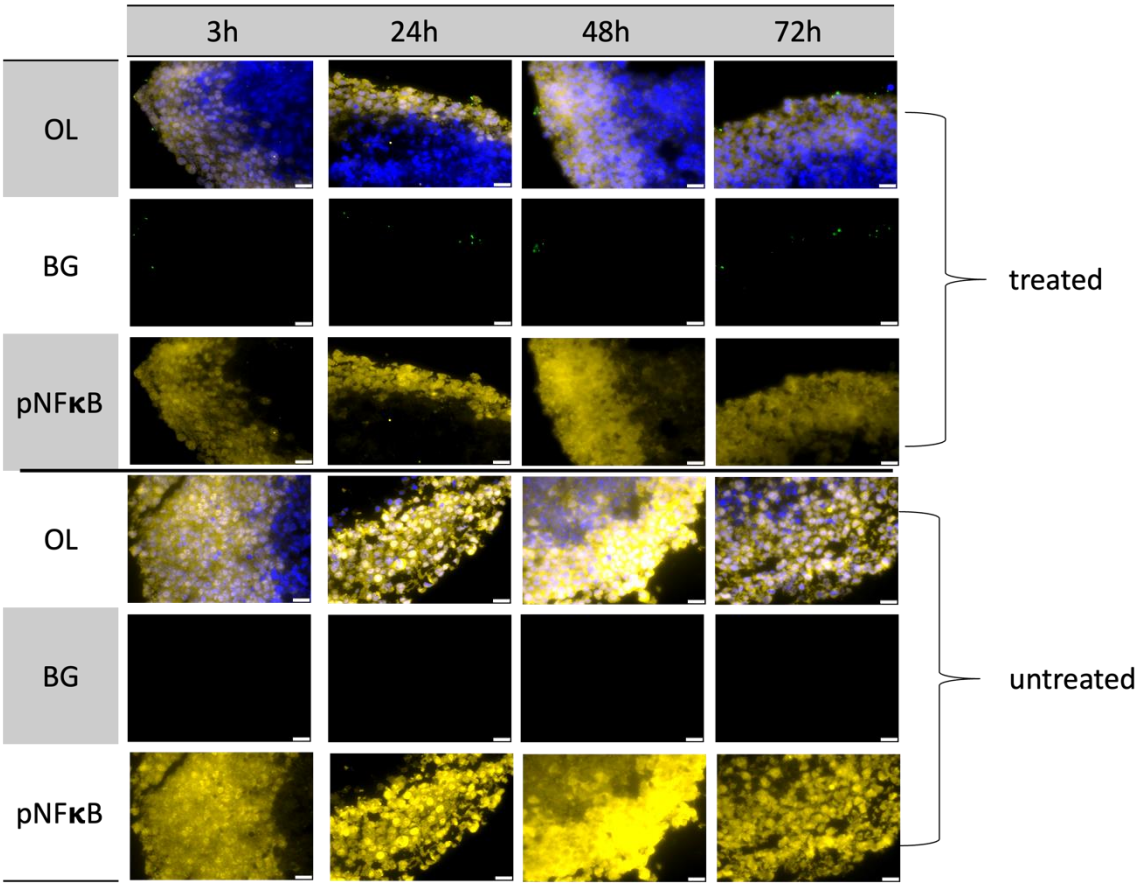

Figure 29: Results of IHC staining – pNFκB *of CT26Luc spheroids treated with AF488-BGs (upper row) and untreated control group (lower row), after different incubation periods (3h, 24h, 48h, 72h), showing one spheroid of n = 2 spheroids. Images taken with fluorescence microscope at 60x-magnification. Green = AF488-BGs with FITC filter; Blue = Hoechst with DAPI filter; Yellow = secondary AB-labelled primary AB for pNFκB with CY3 filter. Bar size = 20 µm, OL = Overlay.*

The IHC staining of IL-6 exposes a clear activation in response to BG-treatment. As illustrated in **Figure 30**, in the treated spheroids IL-6 signals are prominently detectable, correlating with areas of BG integration within the spheroid architecture. In contrast, untreated spheroids exhibit no detectable IL-6 expression.

The spatially restricted expression of IL-6 suggests that IL-6 induction is a direct result of the TLR4 signalling pathway activated by the LPS of BGs (Fitzgerald et al., 2003). As no significant difference in NFκB activation is evident, the IL-6 response is likely triggered by the TRAM-dependent signalling pathway, although cytokine transcription could occur via alternative mediators such as IRF3 or STAT3 (Kawai & Akira, 2010).

The potential effects of upregulated IL-6 through BG treatment are complex, as IL-6 can both enhance immune responses and contribute to tumour progression, depending on the immunological context. On the one hand, IL-6 contributes to the activation of the anti-tumour immune system by supporting antigen presentation and inflammatory cell recruitment (Grivennikov & Karin, 2011), on the other hand, it is also a key driver of JAK/STAT3 signalling, which has been shown to promote CRC cell survival (Kumari et al., 2016). Therefore, although BGs show potential as immunomodulatory agents, their effects on IL-6 signalling pathways should be carefully considered and further investigation is needed to conclude whether pro- or anti-inflammatory response is triggered.

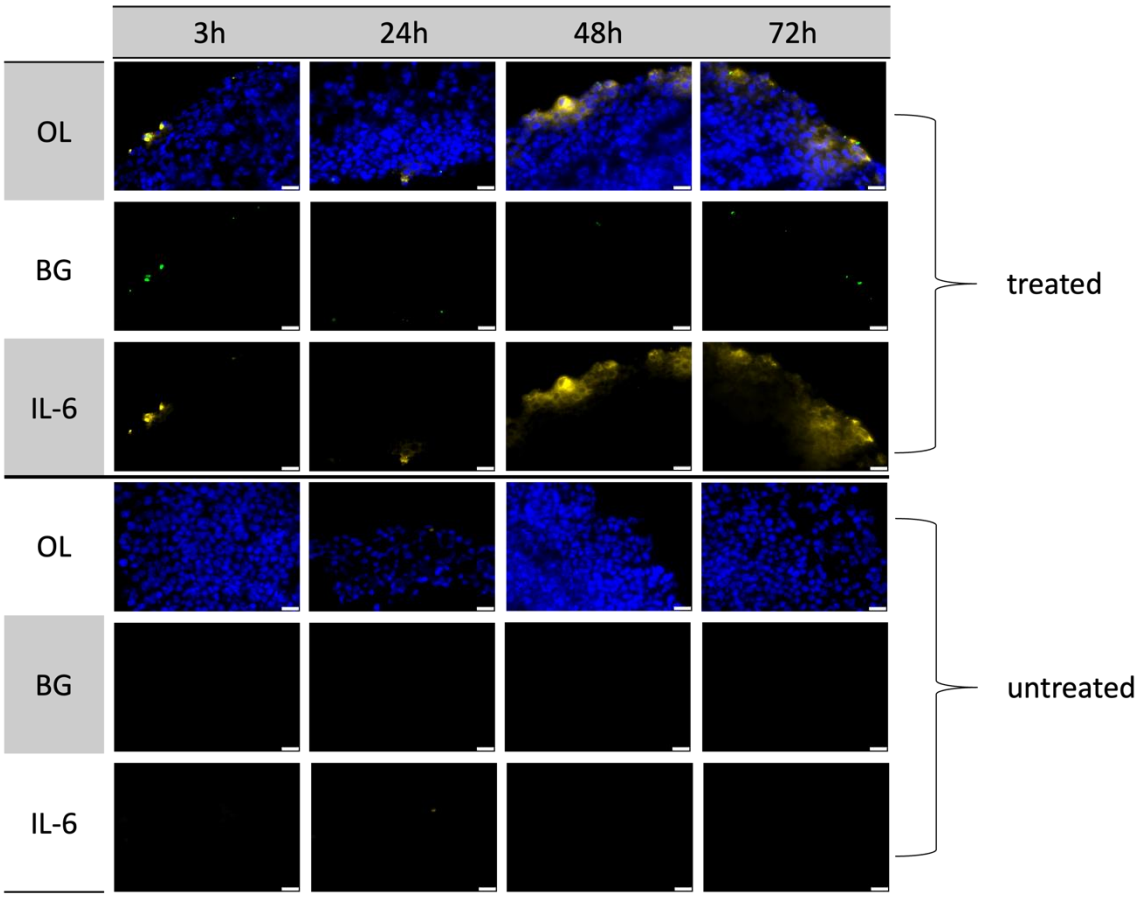

Figure 30: Results of IHC staining – IL-6 *of CT26Luc spheroids treated with AF488-BGs (upper row) and untreated control group (lower row), after different incubation periods (3h, 24h, 48h, 72h), showing one spheroid of n = 2 spheroids. Images taken with fluorescence microscope at 60x-magnification. Green = AF488-BGs with FITC filter; Blue = Hoechst with DAPI filter; Yellow = secondary AB-labelled primary AB for IL-6 with CY3 filter. Bar size = 20 µm, OL = Overlay.*

The IHC analysis of IL-10 reveals the presence of this anti-inflammatory cytokine in both treated and untreated CT26Luc spheroids. As **Figure 31** shows, the fluorescent signals appear rather similar, indicating that IL-10 expression is independent of BG-treatment.

This immunomodulatory cytokine has anti-inflammatory but also tolerogenic effects. It influences the immune response by inhibiting the antigen presentation of dendritic cells and macrophages and by reducing the production of pro-inflammatory cytokines (Mittal et al., 2015). In addition, it promotes the development and function of regulatory T cells (Tregs), which contributes to the development of an immunosuppressive environment (Salkeni & Naing, 2023).

IL-10 can be produced by immune cells, such as T-regulatory cells and tumour-associated macrophages, but also by tumour cells themselves, which can lead to upregulation in the tumour microenvironment. The biological effect of IL-10 in turn depends on various factors. On the one hand, it can dampen chronic inflammation, but on the other hand it also suppresses anti-tumour immune responses as well as the activity of cytotoxic T cells and interferon signalling, which further facilitates the escape from the immune system (Sato et al., 2011).

Since signals are also visible in the untreated spheroids, it can be assumed that the CT26Luc spheroids exhibit immune suppression, for which CRC is well known (Sato et al., 2011). The unchanged IL-10 expression after BG treatment indicates that although BGs trigger a strong proinflammatory response through IL-6, IL-10 mediated immunosuppression is not promoted. This is good from a therapeutic perspective, as high IL-10 levels are associated with reduced anti-tumour immunity and immune-based therapies often have a weaker response (Salkeni & Naing, 2023).

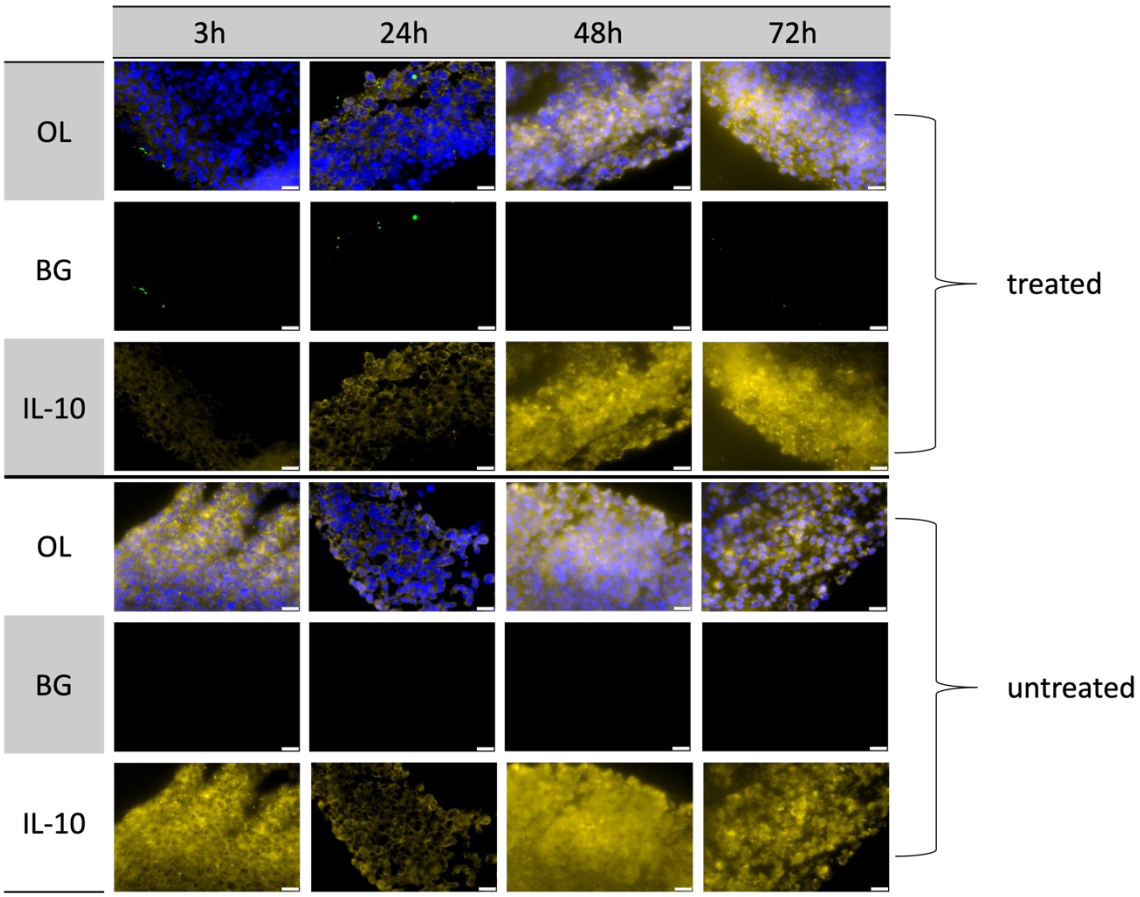

Figure 31: Results of IHC staining – IL-10 *of CT26Luc spheroids treated with AF488-BGs (upper row) and untreated control group (lower row), after different incubation periods (3h, 24h, 48h, 72h), showing one spheroid of n = 2 spheroids. Images taken with fluorescence microscope at 60x-magnification. Green = AF488-BGs with FITC filter; Blue = Hoechst with DAPI filter; Yellow = secondary AB-labelled primary AB for IL-10 with CY3 filter. Bar size = 20 µm, OL = Overlay.*

Figure 32 presents the results of the IHC stained proliferative indicator Ki-67, showing proliferative activity predominantly at the periphery of the spheroids. This supports the zonal organisation of 3D cell culture models described in Chapter 4.2.

At the localizations, where BGs integrated into the spheroids, no Ki-67 signals are visible, suggesting a potential local inhibitory effect on tumour cell proliferation either by disrupting cell cycle progression or by inducing environmental conditions that suppress proliferative capacity. Ki-67 is closely linked to the cell cycle, as it is present in all active phases, but not in G0. For this reason, Ki-67 is a sensitive marker for the proliferation state, but not for growth (Scholzen & Gerdes, 2000). The absence of Ki-67 in BG regions could indicate a shift of the tumour cells to a non-proliferative (G0) or stressed state, but further experiments are required to prove this thesis.

Importantly, despite this localised suppression, the global pattern of Ki-67 distribution remains comparable between treated and untreated spheroids. This finding suggests that the BGs do not cause widespread growth arrest, but rather have a spatially restricted effect, possibly through localised immunostimulatory or structural effects. Such zonal effects have been reported in studies investigating the effects of therapeutic agents or mechanical restraints on tumour spheroids (Mary et al., 2022).

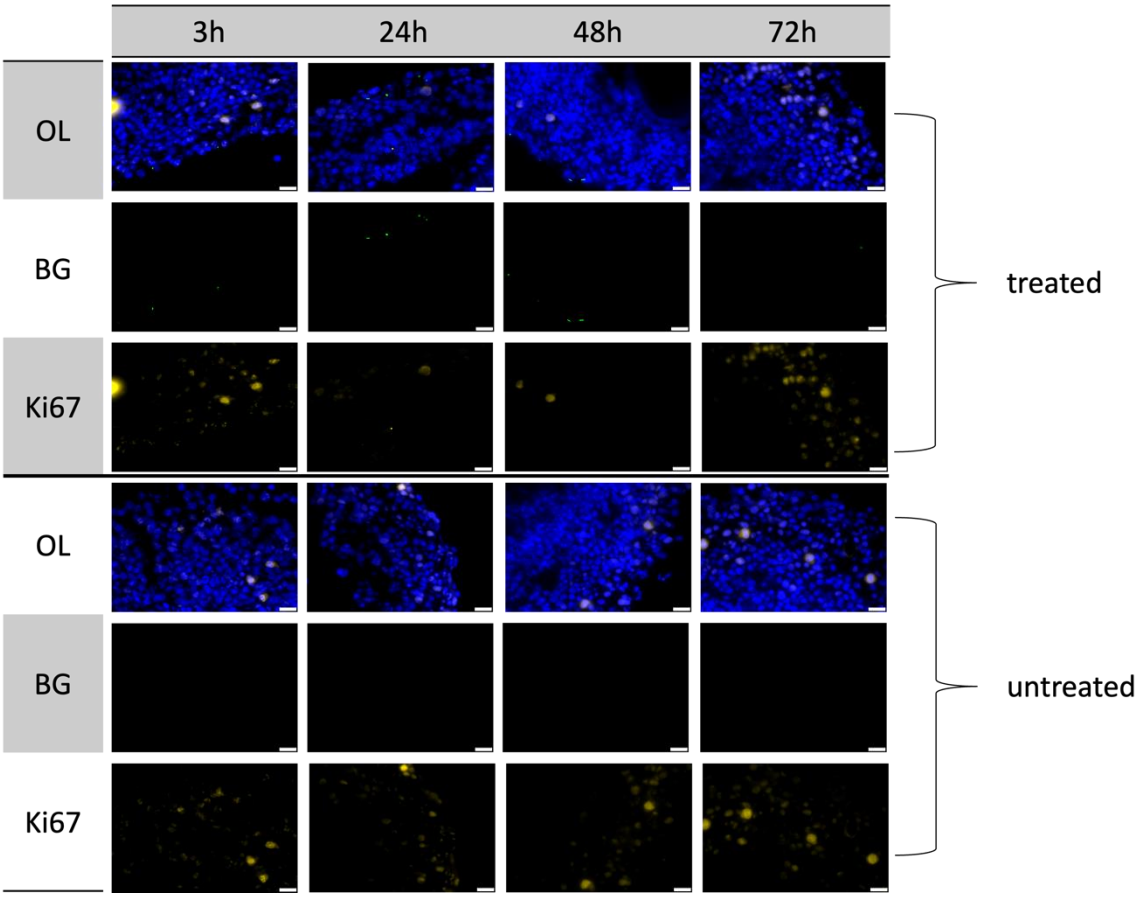

Figure 32: Results of IHC staining – Ki-67 *of CT26Luc spheroids treated with AF488-BGs (upper row) and untreated control group (lower row), after different incubation periods (3h, 24h, 48h, 72h), showing one spheroid of n = 2 spheroids. Images taken with fluorescence microscope at 60x-magnification. Green = AF488-BGs with FITC filter; Blue = Hoechst with DAPI filter; Yellow = secondary AB-labelled primary AB for Ki-67 with CY3 filter. Bar size = 20 µm, OL = Overlay.*

The IHC analysis of BG-treated CT26Luc spheroids confirmed successful internalization of BGs and subsequent activation of key components within the TLR4 signalling pathway. Notably, TRAM and IL-6 were selectively upregulated in response to BG exposure, indicating stimulation of the MyD88-independent cascade. In contrast, pNFκB, IL-10 and Ki-67 showed no differential expression between treated and untreated spheroids.

8 CONCLUSION AND OUTLOOK

This thesis aimed, on the one hand, the optimization of spheroid formation of HT29 and EEC 12Z cell lines and, on the other hand, the investigation of the effect of BG treatment on the TLR4 pathway in CT26Luc spheroids.

Through performing PhC microscopy and RSZ assays, the spheroid formation of HT29 and EEC 12Z was successfully optimized. The colon carcinoma cell line HT29 forms reproducible spheroids with consistent growth patterns and viability across different cell densities, with developing a coronal layer over the time. The necrotic core (stained with PI) forms after approximately one week and increases till it gets the dominant feature within the spheroid in comparison to the amount of living cells (counterstained with Hoechst). Similarly, the epithelial endometriosis cell line EEC 12Z forms spheroids with a very compact morphology without establishing a coronal layer, although their smaller size introduces handling challenges. The formation of the necrotic core starts already on day 3 but plateaus afterwards. The supplementation of gelatine and collagen to the spheroids shows a higher RFU within collagen-treated spheroids, suggesting a positive impact.

Murine colon carcinoma cells CT26Luc were treated with BGs and imaged with the FLM at different timepoints (3h-, 24h-, 48-, and 72h post-incubation) to evaluate the integration of BGs. The results confirm a time-dependent uptake of BGs with increasing accumulation. Afterwards, IHC staining was performed on the sectioned spheroids to investigate the effect on TLR4 pathway using different primary ABs: TLR4, TRAM, pNFκB, IL-6 and IL-10, as well as the marker for proliferation Ki-67. The analysis reveals that BG treatment activates TRAM-dependent TLR4 signalling cascade, which further leads to induction of IL-6 production. As the signal of pNFκB is similar in treated and untreated spheroids, an alternative way must be used to produce inflammatory agents. Furthermore, the presence of TLR4 and IL-10 is shown with no significant impact of the BGs. Moreover, the staining with Ki-67 proves that both treated and untreated spheroids have proliferative cells especially in peripheral areas, with a slight correlation between BG-localisation and the lack of Ki-67 signal in the corresponding area.

In summary, this study confirms that spheroid models are highly suitable for investigating complex tumour-immune interactions and highlights the ability of BGs to selectively active the innate immune signalling via TLR4. Given the dual role of IL-6 in tumour progression and immune activation, future research should focus on refining this approach to improve therapeutic specificity.

The results of this thesis emphasize the promising potential of BGs as adaptable targeted drug delivery systems and immunomodulators, potentially revolutionizing cancer therapy. Their unique capacity to selectively colonize tumours and activate specific immune pathways offers opportunities for personalized drug delivery as well as for the development of cancer vaccines, especially for CRC and potentially beyond.

9 APPENDIX

The following supplementary figures should provide additional information about the necrotic core formation of HT29 and EEC 12Z spheroids, as well as the IHC staining of CT26Luc spheroids treated with BGs, images taken with 20x- and 60x- magnification.

Figure 33A presents the necrotic core formation of HT29 spheroids as separated layers over an 18-days period, demonstrating the progressive increase from day 7 onwards. The corresponding workflow is outlined in Section 6.2.1 with the results discussed in Chapter 7.1.1.

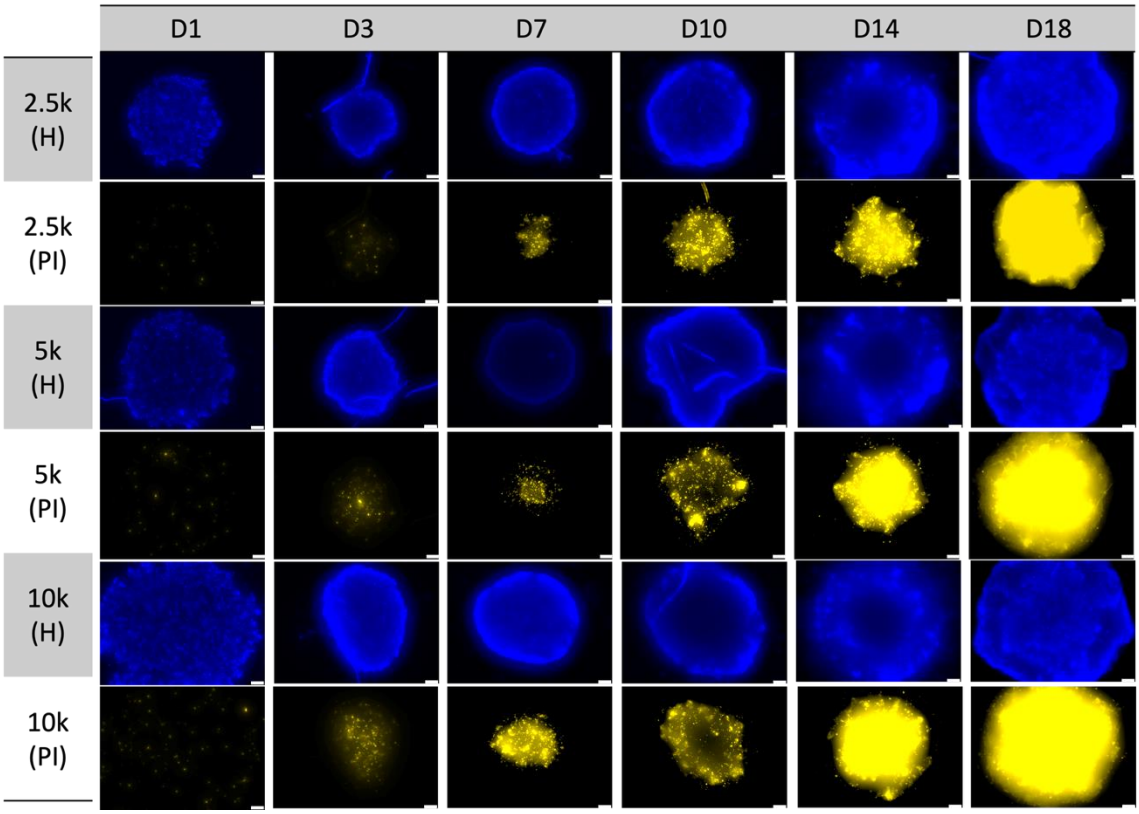

Figure 33A: Necrotic core of HT29 as separated layers *of one spheroid per seeding number imaged with FLM. PI = Propidium iodide (conc. 500 µg/mL, exposure time = 10 ms) with CY3 filter; H = Hoechst (conc. 320 µg/mL, exposure time = 40 ms) with DAPI filter. D = Day, k = thousand*

Figure 34A shows the separated layers of the formed necrotic core within EEC 12Z spheroids over a 16-days period. Already on day 1, several dead cells are visible and on day 3 the necrotic core is the dominant feature within the spheroids but plateauing

afterwards. 6.2.2 provides the workflow and Chapter 7.1.2 the corresponding results and discussion.

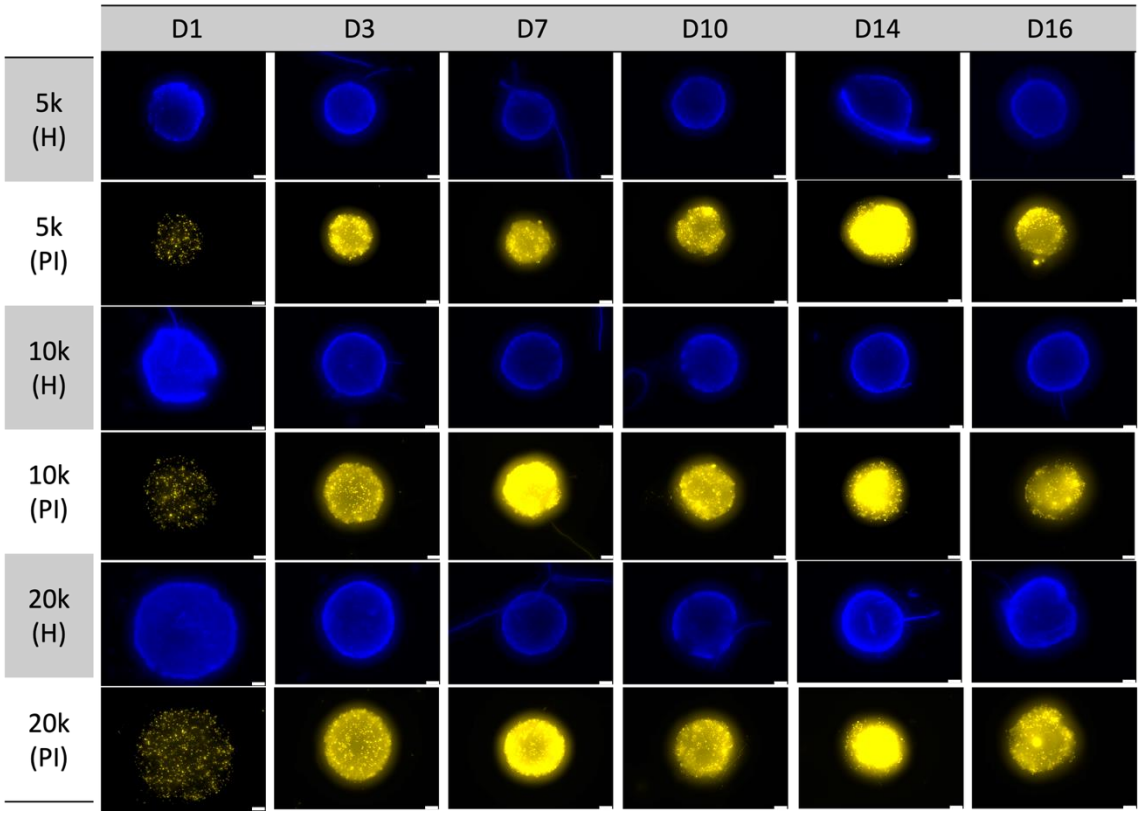

Figure 34A: Necrotic core of EEC 12Z as separated layers *of one spheroid per seeding number imaged with FLM. PI = Propidium iodide (conc. 500 µg/mL, exposure time = 10 ms) with CY3 filter; H = Hoechst (conc. 320 µg/mL, exposure time = 40 ms) with DAPI filter. D = Day, k = thousand*

In the next figures the remaining images from IHC staining of BG-treated CT26Luc spheroids are presented, including the corresponding isotype controls and additional timepoints (24 h, 48 h) captured with the FLM at 20x- and 60x-magnification.

The results of IHC staining after 24 h of incubation (**Figure 35A**) and 48 h of incubation (**Figure 36A**) demonstrate the increasing signal intensity of TLR4, pNFκB and IL-10 in both treated and untreated spheroids, as well as the signals of TRAM and IL-6 only visible in BG-treated spheroids. As Ki67 has weak signal it is not clearly observable with this magnification. These figures present the additional timepoints of IHC staining captured at 20x-magnification with the other two timepoints shown in Chapter 7.2.

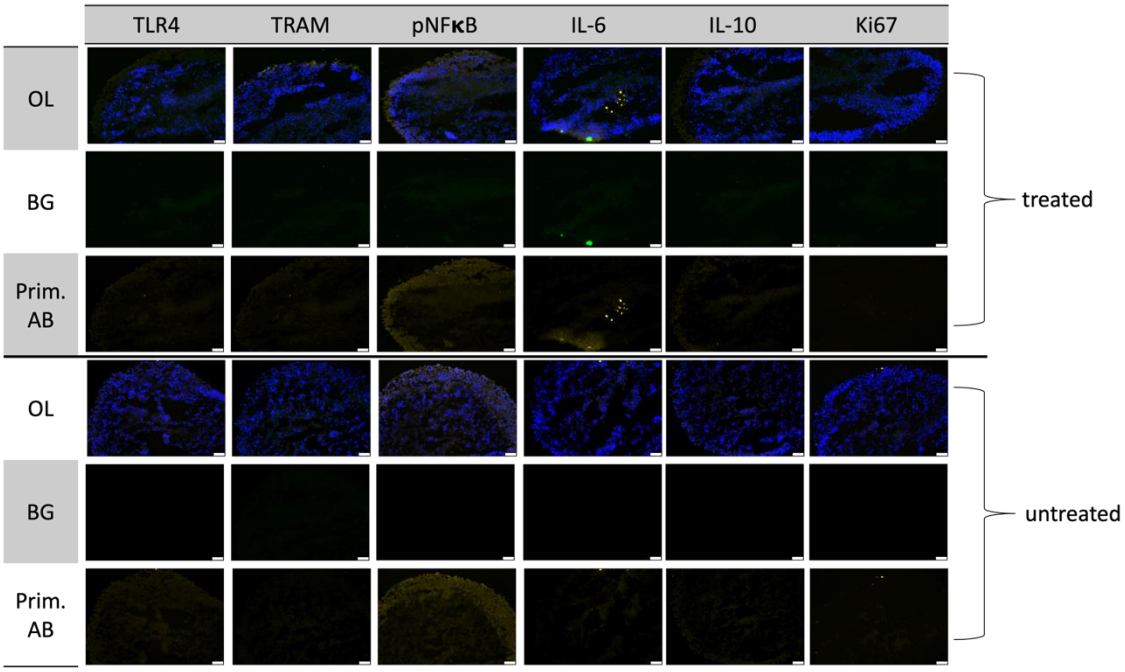

Figure 35A: Results of IHC staining – 24h *of CT26Luc spheroids treated with AF488-BGs (upper row) and untreated control groups (lower row) showing one spheroid of n = 2 spheroids using six different primary antibodies visualized with secondary antibody. Images taken with fluorescence microscope at 20x-magnification. Green = AF488-BGs with FITC filter; Blue = Hoechst with DAPI filter; Yellow = secondary AB with CY3 filter. Bar size = 50 µm, OL = Overlay.*

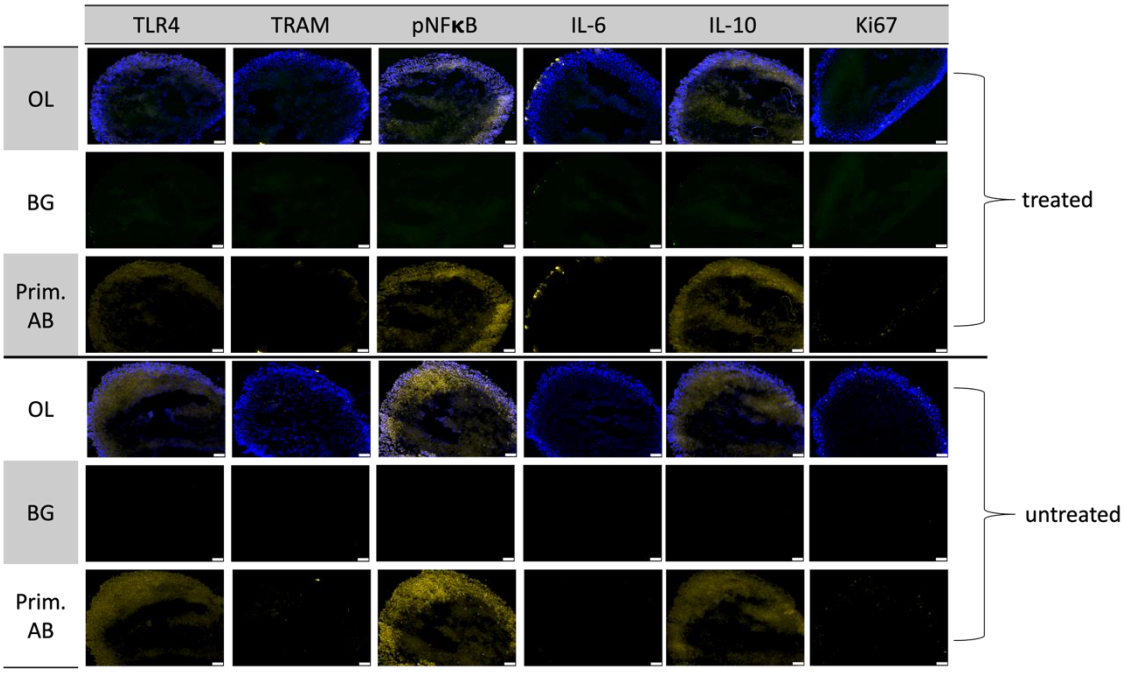

Figure 36A: Results of IHC staining – 48h *of CT26Luc spheroids treated with AF488-BGs (upper row) and untreated control groups (lower row) showing one spheroid of n = 2 spheroids using six different primary antibodies visualized with secondary antibody. Images taken with fluorescence microscope at 20x-magnification. Green = AF488-BGs with FITC filter; Blue = Hoechst with DAPI filter; Yellow = secondary AB with CY3 filter. Bar size = 50 µm, OL = Overlay.*

In the following figures, the associated isotype controls are shown for each IHC staining. These controls aim to reveal any non-specific binding by the primary and secondary AB. The images were subsequently colour-balanced against the isotype controls to minimize background noise until no residual signal was detectable, ensuring genuine antigen-AB-interactions in the results rather than artefacts.

Two isotype control concentrations were used: the higher concentration (8 µg/mL, **Figure 37A**) for all the primary ABs except for Ki67, for which the lower concentrated control (0.4 µg/mL, **Figure 38A**) was used. Since the Ki67 AB expresses weaker fluorescence, the reduced isotype control allows for extended exposure times. Thereby, the Ki67 signal amplifies without introducing background noise. These figures prove that no signals are visible in the control groups, therefore all results seen in Chapter 7.2 are genuine signals of antigen-AB-interactions.

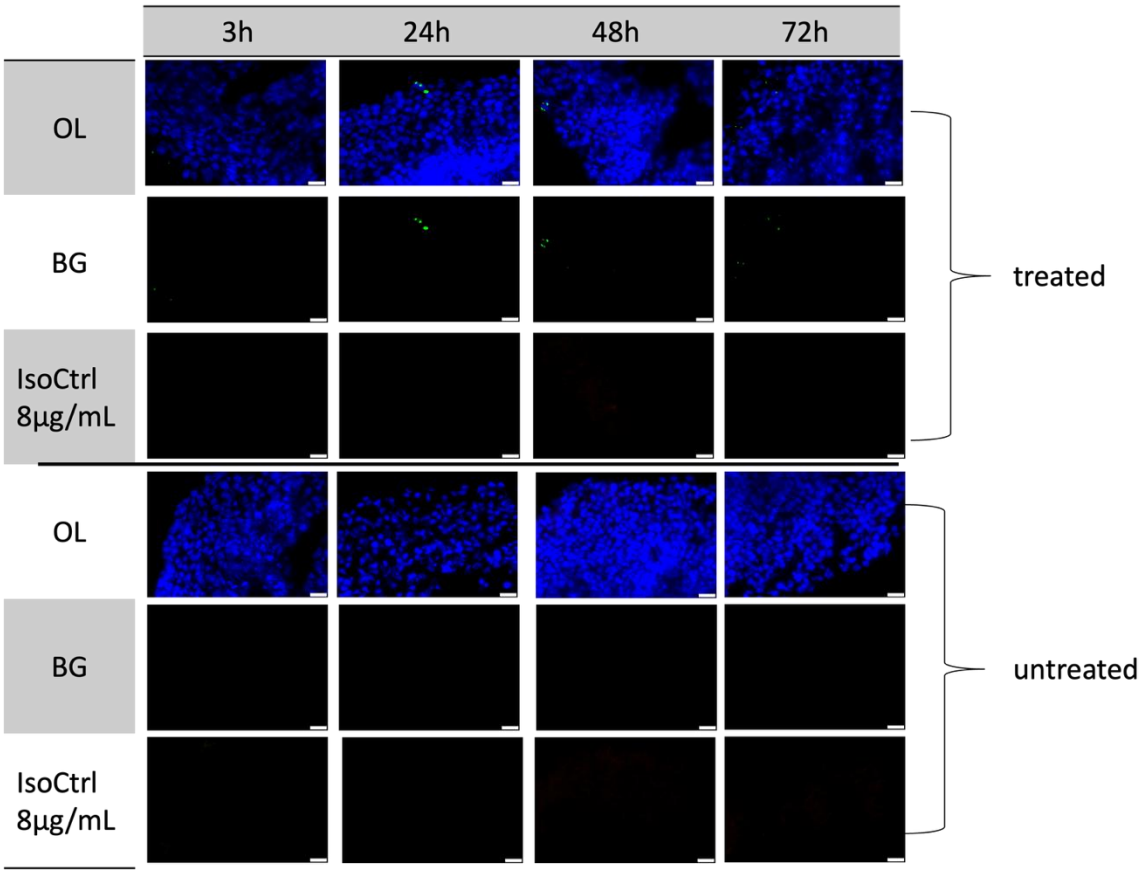

Figure 37A: IHC staining - Isotype control 8 µg/mL *of CT26Luc spheroids treated with AF488-BGs (upper row) and untreated control group (lower row), after different incubation periods (3h, 24h, 48h, 72h), showing one spheroid of n = 2 spheroids. Images taken with fluorescence microscope at 60x-magnification. Green = AF488-BGs with FITC filter; Blue = Hoechst with DAPI filter. Bar size = 20 µm, OL = Overlay.*

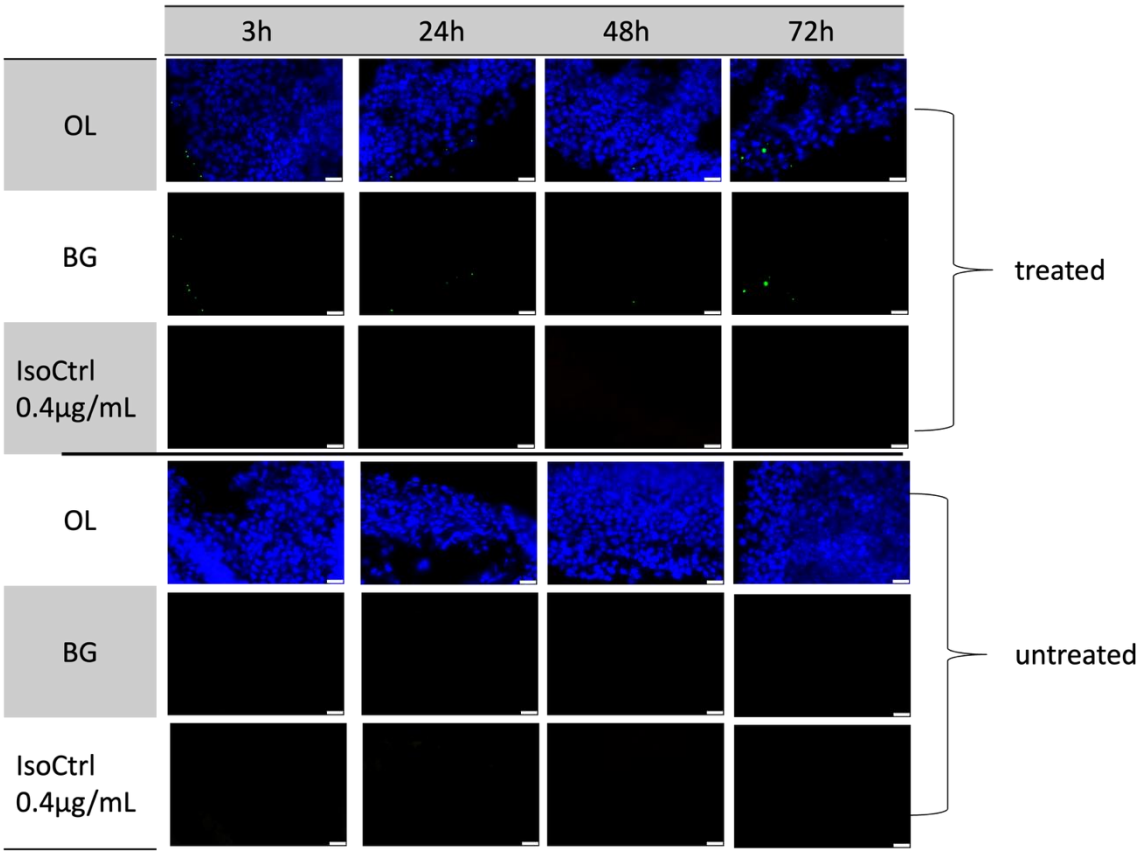

Figure 38A: IHC staining - Isotype control 0,4 µg/mL *of CT26Luc spheroids treated with AF488-BGs (upper row) and untreated control group (lower row), after different incubation periods (3h, 24h, 48h, 72h), showing one spheroid of n = 2 spheroids. Images taken with fluorescence microscope at 60x-magnification. Green = AF488-BGs with FITC filter; Blue = Hoechst with DAPI filter. Bar size = 20 µm, OL = Overlay.*

To complete the experimental series, the second replicate (Set 2) of BG-treated and untreated spheroids from each condition and timepoint is presented, in the following. These additional images underline the results from the main figures (Set 1) described in Chapter 7.2 and further strengthen their validity. Technical problems during the IHC staining of Set 2, most notably the premature loss of DAPI signal before imaging at 60x-magnification, prevented a reliable representation in the "Results and Discussion" Chapter. Furthermore, in some of the images, artefacts appear due to incorrect edit, which should be considered when interpreting the results. The following figures illustrate the results of FLM at 20x-magnification at different timepoints (**Figure 39A** - **Figure 42A**).

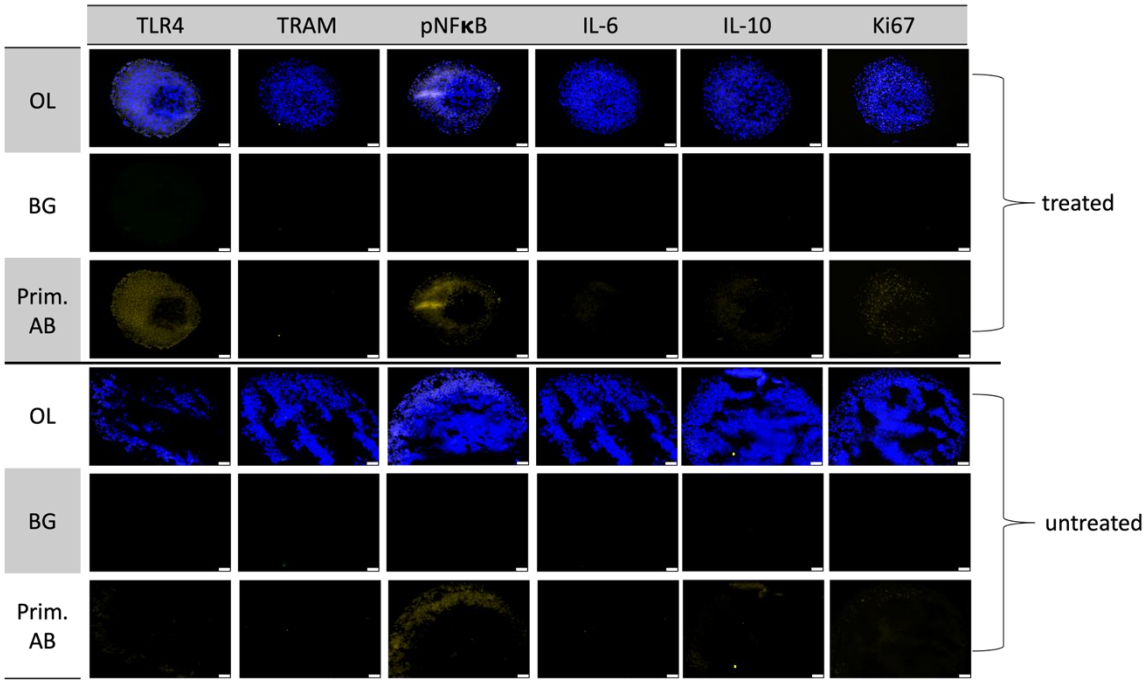

Figure 39A: Results of IHC staining (Set 2) – 3h *of CT26Luc spheroids treated with AF488-BGs (upper row) and untreated control groups (lower row) showing one spheroid of n = 2 spheroids using six different primary antibodies visualized with secondary antibody. Images taken with fluorescence microscope at 20x-magnification. Green = AF488-BGs with FITC filter; Blue = Hoechst with DAPI filter; Yellow = secondary AB with CY3 filter. Bar size = 50 µm, OL = Overlay.*

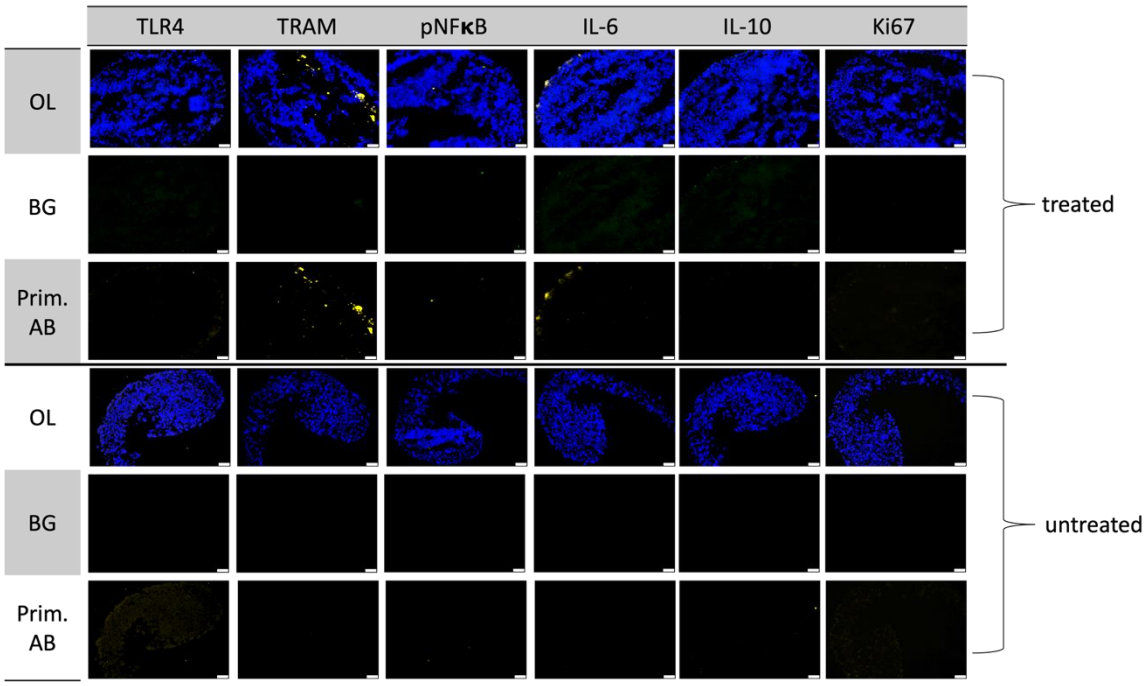

Figure 40A: Results of IHC staining (Set 2) – 24h *of CT26Luc spheroids treated with AF488-BGs (upper row) and untreated control groups (lower row) showing one spheroid of n = 2 spheroids using six different primary antibodies visualized with secondary antibody. Images taken with fluorescence microscope at 20x-magnification. Green = AF488-BGs with FITC filter; Blue = Hoechst with DAPI filter; Yellow = secondary AB with CY3 filter. Bar size = 50 µm, OL = Overlay.*

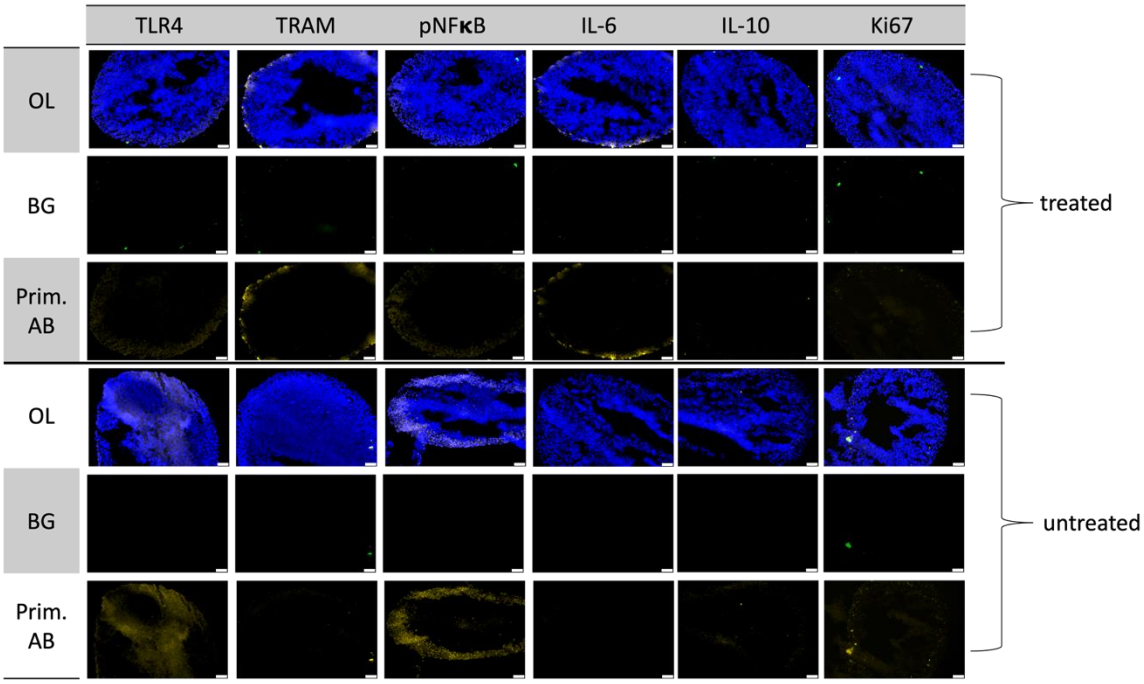

Figure 41A: Results of IHC staining (Set 2) – 48h *of CT26Luc spheroids treated with AF488-BGs (upper row) and untreated control groups (lower row) showing one spheroid of n = 2 spheroids using six different primary antibodies visualized with secondary antibody. Images taken with fluorescence microscope at 20x-magnification. Green = AF488-BGs with FITC filter; Blue = Hoechst with DAPI filter; Yellow = secondary AB with CY3 filter. Bar size = 50 µm, OL = Overlay.*

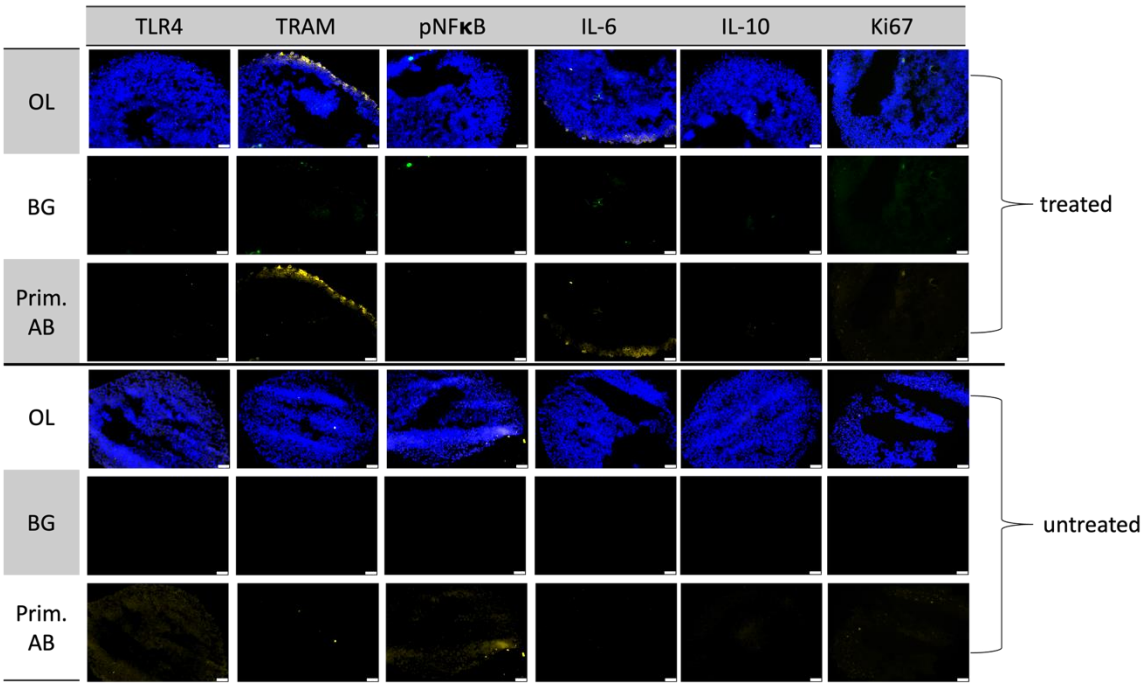

Figure 42A: Results of IHC staining (Set 2) – 72h *of CT26Luc spheroids treated with AF488-BGs (upper row) and untreated control groups (lower row) showing one spheroid of n = 2 spheroids using six different primary antibodies visualized with secondary antibody. Images taken with fluorescence microscope at 20x-magnification. Green = AF488-BGs with FITC filter; Blue = Hoechst with DAPI filter; Yellow = secondary AB with CY3 filter. Bar size = 50 µm, OL = Overlay.*

10 LIST OF FIGURES

11 LIST OF TABLES

12 REFERENCES

Akira, S., & Takeda, K. (2004). Toll-like receptor signalling. In Nature Reviews Immunology (Vol. 4, Issue 7, pp. 499–511). Nature Publishing Group. https://doi.org/10.1038/nri1391

Anwer, M., Bhaliya, K., Munn, A., & Wei, M. Q. (2025). Bacterial ghosts: A breakthrough approach to cancer vaccination. In Biomedicine and Pharmacotherapy (Vol. 182). Elsevier Masson s.r.l. https://doi.org/10.1016/j.biopha.2024.117766

Bissell, M. J., & Hines, W. C. (2011). Why don't we get more cancer? A proposed role of the microenvironment in restraining cancer progression. In Nature Medicine (Vol. 17, Issue 3, pp. 320–329). https://doi.org/10.1038/nm.2328

Chen, H., Ji, H., Kong, X., Lei, P., Yang, Q., Wu, W., Jin, L., & Sun, D. (2021). Bacterial ghosts-based vaccine and drug delivery systems. In Pharmaceutics (Vol. 13, Issue 11). MDPI. https://doi.org/10.3390/pharmaceutics13111892

Chen, J., Wei, Y., Yang, W., Huang, Q., Chen, Y., Zeng, K., & Chen, J. (2022). IL-6: The Link Between Inflammation, Immunity and Breast Cancer. In Frontiers in Oncology (Vol. 12). Frontiers Media S.A. https://doi.org/10.3389/fonc.2022.903800

Choudhury, H., Pandey, M., Saravanan, V., Mun, A. T. Y., Bhattamisra, S. K., Parikh, A., Garg, S., & Gorain, B. (2023). Recent progress of targeted nanocarriers in diagnostic, therapeutic, and theranostic applications in colorectal cancer. In Biomaterials Advances (Vol. 153). Elsevier Ltd. https://doi.org/10.1016/j.bioadv.2023.213556

Costa, E. C., Moreira, A. F., de Melo-Diogo, D., Gaspar, V. M., Carvalho, M. P., & Correia, I. J. (2016). 3D tumor spheroids: an overview on the tools and techniques used for their analysis. In Biotechnology Advances (Vol. 34, Issue 8, pp. 1427–1441). Elsevier Inc. https://doi.org/10.1016/j.biotechadv.2016.11.002

Fitzgerald, K. A., Rowe, D. C., Barnes, B. J., Caffrey, D. R., Visintin, A., Latz, E., Monks, B., Pitha, P. M., & Golenbock, D. T. (2003). LPS-TLR4 signaling to IRF-3/7 and NF-κB involves the toll adapters TRAM and TRIF. Journal of Experimental Medicine, 198(7), 1043–1055. https://doi.org/10.1084/jem.20031023

Friedrich, J., Seidel, C., Ebner, R., & Kunz-Schughart, L. A. (2009). Spheroid-based drug screen: Considerations and practical approach. Nature Protocols, 4(3), 309–324. https://doi.org/10.1038/nprot.2008.226

Gholami, A., Mohkam, M., Soleimanian, S., Sadraeian, M., & Lauto, A. (2024). Bacterial nanotechnology as a paradigm in targeted cancer therapeutic delivery and immunotherapy. In Microsystems and Nanoengineering (Vol. 10, Issue 1). Springer Nature. https://doi.org/10.1038/s41378-024-00743-z

Greenhill, C. J., Rose-John, S., Lissilaa, R., Ferlin, W., Ernst, M., Hertzog, P. J., Mansell, A., & Jenkins, B. J. (2011). IL-6 Trans -Signaling Modulates TLR4-Dependent Inflammatory Responses via STAT3. The Journal of Immunology, 186(2), 1199–1208. https://doi.org/10.4049/jimmunol.1002971

Grivennikov, S. I., & Karin, M. (2010). Inflammation and oncogenesis: a vicious connection. In Current Opinion in Genetics and Development (Vol. 20, Issue 1, pp. 65–71). https://doi.org/10.1016/j.gde.2009.11.004

Groza, D., Gehrig, S., Kudela, P., Holcmann, M., Pirker, C., Dinhof, C., Schueffl, H. H., Sramko, M., Hoebart, J., Alioglu, F., Grusch, M., Ogris, M., Lubitz, W., Keppler, B. K., Pashkunova-Martic, I., Kowol, C. R., Sibilia, M., Berger, W., & Heffeter, P. (2018). Bacterial ghosts as adjuvant to oxaliplatin chemotherapy in colorectal carcinomatosis. OncoImmunology, 7(5). https://doi.org/10.1080/2162402X.2018.1424676

Heine, H., & Riekenberg, S. (2010). Toll-like receptor recognition of lipoglycans, glycolipids and lipopeptides. https://doi.org/10.1016/B978-0-1237-4546-0.00031-6

Hossain, M. S., Karuniawati, H., Jairoun, A. A., Urbi, Z., Ooi, D. J., John, A., Lim, Y. C., Kaderi Kibria, K. M., Mohiuddin, A. K. M., Ming, L. C., Goh, K. W., & Hadi, M. A. (2022). Colorectal Cancer: A Review of Carcinogenesis, Global Epidemiology, Current Challenges, Risk Factors, Preventive and Treatment Strategies. In Cancers (Vol. 14, Issue 7). MDPI. https://doi.org/10.3390/cancers14071732

Huang, Z., & Yang, M. (2022). Molecular Network of Colorectal Cancer and Current Therapeutic Options. In Frontiers in Oncology (Vol. 12). Frontiers Media S.A. https://doi.org/10.3389/fonc.2022.852927

Ijaz, M., Hasan, I., Chaudhry, T. H., Huang, R., Zhang, L., Hu, Z., Tan, Q., & Guo, B. (2024). Bacterial derivatives mediated drug delivery in cancer therapy: a new generation strategy. In Journal of Nanobiotechnology (Vol. 22, Issue 1). BioMed Central Ltd. https://doi.org/10.1186/s12951-024-02786-w

Karin, M., & Greten, F. R. (2005). NF-κB: Linking inflammation and immunity to cancer development and progression. In Nature Reviews Immunology (Vol. 5, Issue 10, pp. 749–759). https://doi.org/10.1038/nri1703

Kawai, T., & Akira, S. (2010). The role of pattern-recognition receptors in innate immunity: Update on toll-like receptors. In Nature Immunology (Vol. 11, Issue 5, pp. 373–384). https://doi.org/10.1038/ni.1863

Kawasaki, T., & Kawai, T. (2014). Toll-like receptor signaling pathways. In Frontiers in Immunology (Vol. 5, Issue SEP). Frontiers Media S.A. https://doi.org/10.3389/fimmu.2014.00461

Kim, H. J., Kim, H., Lee, J. H., & Hwangbo, C. (2023). Toll-like receptor 4 (TLR4): new insight immune and aging. In Immunity and Ageing (Vol. 20, Issue 1). BioMed Central Ltd. https://doi.org/10.1186/s12979-023-00383-3

Kumari, N., Dwarakanath, B. S., Das, A., & Bhatt, A. N. (2016). Role of interleukin-6 in cancer progression and therapeutic resistance. In Tumor Biology (Vol. 37, Issue 9, pp. 11553–11572). Springer Science and Business Media B.V. https://doi.org/10.1007/s13277-016-5098-7

Lu, C. C., Kuo, H. C., Wang, F. S., Jou, M. H., Lee, K. C., & Chuang, J. H. (2014). Upregulation of TLRs and IL-6 as a marker in human colorectal cancer. International Journal of Molecular Sciences, 16(1), 159–177. https://doi.org/10.3390/ijms16010159

Maida, M., Dahiya, D. S., Shah, Y. R., Tiwari, A., Gopakumar, H., Vohra, I., Khan, A., Jaber, F., Ramai, D., & Facciorusso, A. (2024). Screening and Surveillance of Colorectal Cancer: A Review of the Literature. In Cancers (Vol. 16, Issue 15). Multidisciplinary Digital Publishing Institute (MDPI). https://doi.org/10.3390/cancers16152746

Mary, G., Malgras, B., Perez, J. E., Nagle, I., Luciani, N., Pimpie, C., Asnacios, A., Pocard, M., Reffay, M., & Wilhelm, C. (2022). Magnetic Compression of Tumor Spheroids Increases Cell Proliferation In Vitro and Cancer Progression In Vivo. Cancers, 14(2). https://doi.org/10.3390/cancers14020366

Mehta, G., Hsiao, A. Y., Ingram, M., Luker, G. D., & Takayama, S. (2012). Opportunities and challenges for use of tumor spheroids as models to test drug delivery and efficacy. Journal of Controlled Release, 164(2), 192–204. https://doi.org/10.1016/j.jconrel.2012.04.045

Mittal, S. K., Cho, K. J., Ishido, S., & Roche, P. A. (2015). Interleukin 10 (IL-10)-mediated Immunosuppression March-i induction regulates antigen presentation by macrophages but not Dendritic cells. Journal of Biological Chemistry, 290(45), 27158–27167. https://doi.org/10.1074/jbc.M115.682708

Nayak, P., Bentivoglio, V., Varani, M., & Signore, A. (2023). Three-Dimensional In Vitro Tumor Spheroid Models for Evaluation of Anticancer Therapy: Recent Updates. In Cancers (Vol. 15, Issue 19). Multidisciplinary Digital Publishing Institute (MDPI). https://doi.org/10.3390/cancers15194846

Nunes, A. S., Barros, A. S., Costa, E. C., Moreira, A. F., & Correia, I. J. (2019). 3D tumor spheroids as in vitro models to mimic in vivo human solid tumors resistance to therapeutic drugs. In Biotechnology and Bioengineering (Vol. 116, Issue 1, pp. 206–226). John Wiley and Sons Inc. https://doi.org/10.1002/bit.26845

Oblak, A., & Jerala, R. (2011). Toll-like receptor 4 activation in cancer progression and therapy. In Clinical and Developmental Immunology (Vol. 2011). https://doi.org/10.1155/2011/609579

Park, S. Y. (2023). Chemically induced bacterial ghosts: a novel approach for advancing biomedical applications. In Molecular and Cellular Toxicology (Vol. 19, Issue 4, pp. 657–665). Springer Verlag. https://doi.org/10.1007/s13273-023-00389-4

Pikarsky, E., Porat, R. M., Stein, I., Abramovitch, R., Amit, S., Kasem, S., Gutkovich-Pyest, E., Urieli-Shoval, S., Galun, E. & Ben-Neriah, Y. (2004). NF-κB functions as a tumour promoter in inflammation-associated cancer. Nature, 431(7007), 461–466. https://doi.org/10.1038/nature02924

Radford, G. A., Vrbanac, L., de Nys, R. T., Worthley, D. L., Wright, J. A., Hasty, J., & Woods, S. L. (2024). Towards Understanding Tumour Colonisation by Probiotic Bacterium E. coli Nissle 1917. In Cancers (Vol. 16, Issue 17). Multidisciplinary Digital Publishing Institute (MDPI). https://doi.org/10.3390/cancers16172971

Rawla, P., Sunkara, T., & Barsouk, A. (2019). Epidemiology of colorectal cancer: Incidence, mortality, survival, and risk factors. In Przeglad Gastroenterologiczny (Vol. 14, Issue 2, pp. 89–103). Termedia Publishing House Ltd. https://doi.org/10.5114/pg.2018.81072

Roper, S. J., Linke, F., Scotting, P. J., & Coyle, B. (2021). 3D spheroid models of paediatric SHH medulloblastoma mimic tumour biology, drug response and metastatic dissemination. Scientific Reports, 11(1). https://doi.org/10.1038/s41598-021-83809-6

Salasar Moghaddam, F., Tabibian, M., Absalan, M., Tavoosidana, G., Ghahremani, M. H., Tabatabaei, N., Abdolhosseini, M., Shafiee Sabet, M., & Motevaseli, E. (2024). Comparative analysis of Escherichia coli Nissle 1917 ghosts quality: a study of two chemical methods. Archives of Microbiology, 206(9). https://doi.org/10.1007/s00203-024-04095-0

Salkeni, M. A., & Naing, A. (2023). Interleukin-10 in cancer immunotherapy: from bench to bedside. In Trends in Cancer (Vol. 9, Issue 9, pp. 716–725). Cell Press. https://doi.org/10.1016/j.trecan.2023.05.003

Sato, T., Terai, M., Tamura, Y., Alexeev, V., Mastrangelo, M. J., & Selvan, S. R. (2011). Interleukin 10 in the tumor microenvironment: A target for anticancer immunotherapy. Immunologic Research, 51(2–3), 170–182. https://doi.org/10.1007/s12026-011-8262-6

Scholzen, T., & Gerdes, J. (2000). The Ki-67 protein: From the known and the unknown. In Journal of Cellular Physiology (Vol. 182, Issue 3, pp. 311–322). https://doi.org/10.1002/(SICI)1097-4652(200003)182:3<311::AID-JCP1>3.0.CO;2-9

Xie, Y. H., Chen, Y. X., & Fang, J. Y. (2020). Comprehensive review of targeted therapy for colorectal cancer. In Signal Transduction and Targeted Therapy (Vol. 5, Issue 1). Springer Nature. https://doi.org/10.1038/s41392-020-0116-z

Yamamoto, M., Sato, S., Hemmi, H., Uematsu, S., Hoshino, K., Kaisho, T., Takeuchi, O., Takeda, K., & Akira, S. (2003). TRAM is specifically involved in the Toll-like receptor 4-mediated MyD88-independent signaling pathway. Nature Immunology, 4(11), 1144–1150. https://doi.org/10.1038/ni986